

What dominates the seasonal predictable signals of the East Asian summer monsoon rainfall in addition to the decaying/developing El Niño–Southern Oscillation and spring Arctic Oscillation?

Kairan Ying (✉ yingkr@tea.ac.cn)

Institute of Atmospheric Physics Chinese Academy of Sciences <https://orcid.org/0000-0002-4214-3507>

Dabang Jiang

Institute of Atmospheric Physics Chinese Academy of Sciences

Xiaogu Zheng

Institute of Atmospheric Physics Chinese Academy of Sciences

Carsten S. Frederiksen

Australian Bureau of Meteorology

Jing Peng

Institute of Atmospheric Physics Chinese Academy of Sciences

Tianbao Zhao

Institute of Atmospheric Physics Chinese Academy of Sciences

Linhao Zhong

National Institute of Natural Hazards

Research Article

Keywords: East Asian summer monsoon, precipitation, seasonal forecasting, predictability

Posted Date: May 9th, 2022

DOI: <https://doi.org/10.21203/rs.3.rs-1557627/v1>

License:  This work is licensed under a Creative Commons Attribution 4.0 International License.

[Read Full License](#)

What dominates the seasonal predictable signals of the East Asian summer monsoon rainfall in addition to the decaying/developing El Niño–Southern Oscillation and spring Arctic Oscillation?

1

Kairan Ying¹, Dabang Jiang^{1,2}, Xiaogu Zheng¹, Carsten S. Frederiksen^{3,4,5},

Jing Peng¹, Tianbao Zhao¹, Linhao Zhong^{2,1}

2 *¹Institute of Atmospheric Physics, Chinese Academy of Sciences, Beijing, China*

3 *²National Institute of Natural Hazards, Ministry of Emergency Management of China,*

4 *Beijing, China*

5 *³The Bureau of Meteorology, Melbourne, Australia*

6 *⁴The School of Earth, Atmosphere and Environment, Monash University,*

7 *Clayton, Victoria, Australia*

8 *⁵CSIRO Oceans and Atmosphere, Aspendale, Australia*

9

(Submitted to Climate Dynamics)

*Corresponding author: Dr. Kairan Ying, yingkr@tea.ac.cn

Abstract

10

11 Improvement in the seasonal forecasting of East Asian summer monsoon rainfall
12 (EASMR) remains a great challenge, as it is influenced by varied and complex
13 impacts from (1) external forcings and slowly varying internal variabilities, which are
14 potentially predictable, and (2) internal dynamics on intraseasonal time scales, which
15 is basically unpredictable beyond a season. In this work, a (co-)variance
16 decomposition method is applied to identify the leading potentially predictable (slow)
17 patterns of the EASMR [the seasonal mean rainfall in the region (100°E–140°E,
18 5°N–50°N) in June–July–August] during 1979–2019 by separating the unpredictable
19 noise (intraseasonal). We focus on the most critical predictable sources that are
20 additional to the decaying (DC) El Niño–Southern Oscillation (ENSO), developing
21 (DV) ENSO, and spring Arctic Oscillation (AO) – the three most important and
22 well-recognized predictors for EASMR. We find that (1) the indices that represent the
23 EASMR predictability related to the DC ENSO, spring AO and DV ENSO are the
24 preceding November to March Niño 1+2 sea surface temperature (SST), the
25 April–May AO, and the May Niño 4 SST, respectively; (2) the dominant additional
26 predictable EASMR signals that are linearly independent of the DC ENSO, spring AO
27 and DV ENSO have apparent relationships with the interannual variability of the SST
28 in the western North Pacific, tropical and southern Atlantic, southern Indian, and
29 Arctic oceans during boreal springtime, as well as the linear trend; and (3) by
30 applying a principal component regression scheme to evaluate the EASMR
31 predictability arising from DC/DV ENSO–AO and these additional predictors, the
32 cross-validated fraction variance skill of the total seasonal mean EASMR is 11%
33 (8%–land; 13%–ocean) for the former, and 15% (15%–land; 15%–ocean) for the latter,
34 with a total of 26% that comprises more than 80% of the potential predictability of the
35 EASMR. The considerable skill stemming from the predictors additional to DC/DV
36 ENSO–AO indicates that they are worthy of attention in the seasonal forecasting of
37 EASMR, especially for terrestrial areas.

38 **Keywords** East Asian summer monsoon • precipitation • seasonal forecasting •
39 predictability

40 **1 Introduction**

41 East Asian summer monsoon rainfall (EASMR) – the rainfall in the region
42 (100°–140°E, 5°–50°N) that is most associated with the East Asian monsoon during
43 boreal summer (June–July–August) – is the major source of water for a broad, highly
44 populous, and agriculturally important region (Wang and LinHo 2002; Ding and Chan
45 2005). How to improve the prediction of the interannual variation in EASMR has
46 attracted a great deal of interest amongst scientists. It is generally accepted that
47 improvements in the seasonal forecasting of EASMR require a clear understanding
48 regarding the sources of predictability (Wang et al. 2008b; Fan et al. 2012; Wu and Yu
49 2016; Takaya et al. 2021).

50 Aimed at understanding the main sources of EASMR seasonal predictability,
51 statistical–empirical methods have been widely applied in many previous studies.
52 Among these, a considerable number of prognostic experiments for predicting East
53 Asian summer monsoon (EASM) indices have been carried out to identify the critical
54 seasonal predictors of EASMR. For example, statistical seasonal prediction schemes
55 developed by Wu et al. (2009a), Wu and Yu (2016) and Jin and Huo (2018) for the
56 EASM index of Wang and Fan (1999); Wang et al. (2013)’s empirical prediction
57 model for the western Pacific subtropical high index; and Zheng et al. (2016)’s
58 statistical prediction model for the EASM index of Li and Zeng (2002). These studies
59 indicated that the decaying (DC) El Niño–Southern Oscillation (ENSO), developing
60 (DV) ENSO, and spring Arctic Oscillation (AO) are the most significant predictors
61 for the seasonal forecasting of EASMR.

62 The key predictable sources of EASMR from ENSO in its DC and DV phases
63 and the spring AO have been widely confirmed by empirical orthogonal function
64 (EOF) analysis studies. For instance, DC ENSO has been identified to be related to
65 the first EOF mode (EOF1) of six combined variables of rainfall and circulations over
66 the EASM region (Wang et al. 2008b), the EOF1 of southern EASMR (Xing et al.
67 2016), the EOF1 of eastern China summer rainfall (Ying et al. 2017), the EOF2 of
68 northern EASMR (Yim et al. 2016), and the EOF2 of Asian summer monsoon rainfall

69 (Wang et al. 2015). Meanwhile, DV ENSO has been found to be linked with the
70 EOF1 of Asian summer monsoon rainfall (Wang et al. 2015), the EOF2 of six
71 combined variables of rainfall and circulations in the EASM region (Wang et al.
72 2008b), the EOF2 of southern EASMR (Xing et al. 2016), and the EOF3 of northern
73 EASMR (Yim et al. 2016). The spring AO has been identified to be associated with
74 the EOF1 of Asian summer monsoon rainfall (Wang et al. 2015). Across this body of
75 work, the leading EASMR patterns, which explain the largest percentage of variance,
76 have been examined to understand the dominant sources of predictability.

77 Dynamical predictions provide another important tool in understanding the
78 predictability of EASMR. It is generally recognized that dynamical prediction using
79 multi-model ensembles yields superior forecasts compared to any single model (Wang
80 et al. 2008a). Based on an ensemble of climate models, it was found that the skill for
81 predicting EASMR derives mainly from the impact of DC and DV ENSO (Yang et al.
82 2008; Lee et al. 2015; Takaya et al. 2021). This may be due to the fact that
83 ENSO-related atmospheric circulations, which transfer the predictable signals from
84 the remote eastern tropical Pacific Ocean to East Asia, are relatively well reproduced
85 in numerical model simulations (Liu et al. 2019).

86 Although these precursory signals in the form of DC/DV ENSO and spring
87 AO are of vital importance for the seasonal prediction of EASMR, it is clear that other
88 factors must also be involved. For example, the record-breaking hot and dry
89 conditions in East Asia in summer 1994 (Park and Schubert 1997; Guan and
90 Yamagata 2003) and the extreme heavy rainfall along the Yangtze River in summer
91 2020 (Li et al. 2021; Zhang et al. 2021; Zhou et al. 2021) both occurred when neither
92 eastern tropical Pacific sea surface temperature (SST) anomalies nor the AO provided
93 a viable forcing mechanism. In fact, as indicated by many earlier studies, the SST
94 anomalies over the Indo-Pacific warm pool (Wang et al. 2015; Xing et al. 2016),
95 Indian Ocean (e.g., the Indian Ocean Basin Mode or Indian Ocean Dipole Mode; Li et
96 al. 2008; Liu et al. 2019), equatorial western North Pacific (Yim et al. 2016),
97 Kuroshio (Ying et al. 2017), northern (Rong et al. 2010) and southern (Jin and Huo

98 2018) Atlantic Ocean, as well as the prolonged linear trend (Wang et al. 2015; Ying et
99 al. 2017), are possible additional sources of EASMR predictability.

100 However, despite the large number of statistical and dynamical studies, the
101 hindcast skill of both statistical schemes and multi-model ensembles remains
102 generally limited when forecasting the seasonal precipitation anomalies over the
103 majority of the East Asian monsoon area (100° – 140° E, 5° – 50° N). Moreover, there is
104 an obvious regional dependence, with higher skill over the tropics than the
105 extra-tropics, as well as over ocean areas compared with land (Wang et al. 2015; Xing
106 et al. 2016; Yim et al. 2016; Liu et al. 2019). This lack of skill in EASMR hindcasts
107 can be partly attributed to (1) the prediction uncertainties from the variability within a
108 season (Zheng and Frederiksen 2004), especially in the extra-tropics; (2) the various
109 predictable sources of EASMR originating from external forcings (such as the SST in
110 the global ocean; Wang et al. 2015) and the slowly varying internal variability in the
111 atmosphere (such as the AO; He et al. 2017); and (3) the complexity of the
112 interactions among the most influential of the predictors – for instance, the AO and
113 the SST anomalies over the Kuroshio current region, the western Pacific warm pool,
114 the tropical Atlantic Ocean, and the Indian Ocean, which are all, to a certain degree,
115 related to ENSO (Wang et al. 2000; Wang et al. 2016).

116 However, most previous studies on seasonal EASMR predictability have only
117 examined the total seasonal mean field, and this includes the influences from slowly
118 varying forcings, which are potentially predictable, and intraseasonal variability,
119 which is essentially unpredictable. As indicated in the literature, there is a substantial
120 component of annual variance arising from the intraseasonal variability (or
121 unpredictable noise), especially in the extra-tropics (Frederiksen and Zheng 2004;
122 Zheng and Frederiksen 2004; Grainger et al. 2017; Ying et al. 2017). Thus, to focus
123 on the predictable signals and the sources of predictability, it is necessary to separate
124 the intraseasonal or unpredictable component as a first step in the analysis. Also, most
125 studies have only looked at the various influences in isolation, without fully
126 considering the complexity of linkages among the predictable factors. For instance, by
127 removing the influential impact from DC/DV ENSO, is there any significant

128 additional EASMR forecasting skill from the SST predictors in the western Pacific,
129 Atlantic and Indian oceans that are closely linked to ENSO? And what are the most
130 important additional predictors of EASMR other than DC/DV ENSO and the spring
131 AO? These questions form the focus of this paper.

132 By separating out the unpredictable component, the aim of this work is to
133 identify the potentially predictable EASMR signals within a unified framework –
134 focusing on those that are additional to DC/DV ENSO and the spring AO. The
135 primary question we attempt to answer is what are the most important additional
136 sources of EASMR predictability besides DC/DV ENSO and the spring AO?
137 However, we also seek to quantify the relative contributions to the predictability of
138 EASMR from DC/DV ENSO and the spring AO and any identified additional sources.
139 To achieve this, we propose identifying the dominant predictable patterns of EASMR
140 that are linearly independent of DC ENSO, DV ENSO and the spring AO. This is
141 done by (1) removing the DC/DV ENSO and spring AO–related variations from the
142 EASMR time series from a predictability perspective; and then (2) separating the
143 modes of interannual variability in the predictable (slow) and unpredictable
144 (intraseasonal) components, respectively, using the (co-)variance decomposition
145 methodology of Zheng and Frederiksen (2004). This (co-)variance decomposition
146 approach has been widely used for various climatic factors to identify predictable
147 modes that generally have larger seasonal potential predictability and are better
148 correlated with the slowly varying internal atmospheric dynamics and external
149 forcings than the patterns derived from the total seasonal mean fields (e.g., Zheng and
150 Frederiksen 2006; Frederiksen et al. 2014; Grainger et al. 2017; Ying et al. 2017). A
151 better understanding of the critical sources of EASMR predictability, particularly
152 those additional to DC/DV ENSO and the spring AO, will provide an excellent way to
153 improve the seasonal forecasting of EASMR. As demonstrated in this paper, by using
154 the identified additional predictors, the skill in predicting EASMR is larger than with
155 the DC/DV ENSO–AO–only prediction scheme, especially over terrestrial regions –
156 the most important but also the most complex and difficult areas of East Asia with
157 respect to climate prediction.

158 The structure of this paper is as follows: The data and methods are introduced in
159 Section 2. The indices that best represent the predictive characteristics in the
160 dominant three predictable EASMR modes sourced from the DC ENSO, spring AO
161 and DV ENSO are identified in Section 3. The dominant sources of predictability of
162 the leading four residual predictable EASMR patterns additional to DC/DV
163 ENSO–AO are presented in Section 4. The proposed principal-component regression
164 analysis for EASMR seasonal forecasting, using all the predictors, is documented in
165 Section 5. Further discussion on the methods, data and results, as well as an overall
166 summary of the study, is provided in Section 6.

167 **2 Data and methods**

168 **2.1 Data**

169 The data used in this study include: (1) monthly precipitation data (on a
170 $2.5^\circ \times 2.5^\circ$ grid) from the Global Precipitation Climatology Project, version 2.3
171 (GPCP; Adler et al. 2003), the Climate Prediction Center Merged Analysis of
172 Precipitation (CMAP; Xie and Arkin 1997) and the National Oceanic and
173 Atmospheric Administration’s Precipitation Reconstruction (PREC; Chen et al. 2002),
174 for the period 1979–2020, all of which are broadly used global (land and ocean)
175 precipitation datasets derived from a mix of satellite estimates over ocean and land
176 and rain gauge measurements from land and atolls; (2) monthly mean specific
177 humidity, the zonal and meridional wind field (at 1000, 925, 850, 700, 600, 500, 400
178 and 300 hPa), sea level pressure, and the 500 hPa geopotential height from the
179 National Centers for Environmental Prediction–National Center for Atmospheric
180 Research Reanalysis 1 project (Kalnay et al. 1996), with a horizontal grid resolution
181 of $2.5^\circ \times 2.5^\circ$ for the same 42-year period; (3) monthly mean SST (on a $1^\circ \times 1^\circ$ grid)
182 from the UK Met Office Hadley Center Sea Ice and Sea Surface Temperature dataset
183 1 (Rayner et al. 2003) for the same 42-year period; and (4) monthly mean climate

184 indices from the National Oceanic and Atmospheric Administration's Climate
185 Prediction Center (<https://www.esrl.noaa.gov/psd/data/climateindices/list/>) for the
186 same 42-year period, including the following Niño SST indices (Trenberth 1997): the
187 Niño 1+2 index [extreme eastern tropical Pacific SST within (90°–80°W, 0°–10°S)],
188 Niño 3 index [eastern tropical Pacific SST within (150°–90°W, 5°N–5°S)], Niño 4
189 index [central tropical Pacific SST within (160°E–150°W, 5°N–5°S)], and Niño 3.4
190 index [east-central tropical Pacific SST within (170°–120°W, 5°N–5°S)], as well as
191 the North Atlantic Oscillation (NAO; Barnston and Livezey 1987) and AO index
192 (Higgins et al. 2002).

193 **2.2 Methods**

194 **2.2.1 Separating the DV/DC ENSO–AO related series and the residual EASMR** 195 **series**

196 Linear regression is applied to estimate the residual component of the monthly
197 mean precipitation at each grid point in the EASMR region. The preceding November
198 to March Niño 1+2 SST, the May Niño 4 SST and the April–May AO are chosen as
199 indices to represent the precursors of the EASMR variability arising from the DC
200 ENSO, DV ENSO and spring AO, respectively (see Section 3 for more detailed
201 discussion). In this way, the rainfall series at each grid point is split into two
202 statistically independent series, i.e., the DC/DV ENSO–AO–related series (DC/DV
203 ENSO–AO–related EASMR) and the residual series (residual EASMR).

204 **2.2.2 Identifying the seasonal predictable and unpredictable components**

205 The (co-)variance decomposition method of Zheng and Frederiksen (2004) is
206 proposed for deriving the spatial patterns of interannual variability in seasonal mean
207 fields related to the variability of predictable (or slow) and unpredictable (or
208 intraseasonal) components, based on monthly mean data. Firstly, the annual cycle is
209 removed from the data. A conceptual model for monthly values of a climate variable

210 in month m ($m = 1, 2, 3$; m is in a specific season) and in year y ($y = 1, \dots, Y$, where Y
 211 is the total number of years) is expressed as

$$212 \quad x_{ym} = \mu_y + \varepsilon_{ym}. \quad (1)$$

213 That is, after removing the annual cycle from the monthly mean data, a monthly
 214 climate variable x_{ym} in month m from a specific three-month season ($m = 1, 2, 3$)
 215 and in year y from the total Y years ($y = 1, \dots, Y$) can be conceptually decomposed into
 216 two components: (1) μ_y , which represents the seasonal “population” mean; and (2)
 217 ε_{ym} , which is related to month-to-month fluctuations. Then, a three-month seasonal
 218 mean (represented by the subscript o) of a climate variable can be conceptually
 219 expressed as

$$220 \quad x_{yo} = \mu_y + \varepsilon_{yo}, \quad (2)$$

221 where ε_{yo} is the intraseasonal component, which is essentially unpredictable beyond
 222 a season, and μ_y is the predictable component, which is dominated by the external
 223 forcing and slowly varying internal dynamics, and is potentially predictable on
 224 seasonal or longer time scales.

225 In the statistical technique of Zheng and Frederiksen (2004), the interannual
 226 (co-)variance of the predictable components $V(\mu_y, \mu'_y)$ can be calculated as

$$227 \quad V(\mu_y, \mu'_y) = V(x_{yo}, x'_{yo}) - V(\varepsilon_{yo}, \varepsilon'_{yo}). \quad (3)$$

228 Here, $V(x_{yo}, x'_{yo})$ represents the total interannual (co-)variance and can be estimated
 229 directly from seasonal mean variables x_{yo} , and $V(\varepsilon_{yo}, \varepsilon'_{yo})$ is the interannual
 230 (co-)variance of the unpredictable components and can be calculated with monthly
 231 data by using Eq. (16) in Zheng and Frederiksen (2004) as follows:

$$232 \quad V(\varepsilon_{yo}, \varepsilon'_{yo}) = \hat{\sigma}^2 (3 + 4\hat{\phi}) / 9, \quad (3.1)$$

233 where

$$234 \quad \hat{\sigma}^2 = \frac{a}{2(1-\phi)}, \quad (3.2)$$

235
$$\hat{\phi} = \min\{0.1, \max[(a + 2b) / (2a + 2b), 0]\}, \quad (3.3)$$

236
$$a = \frac{1}{2} \left\{ \frac{1}{Y} \sum_{y=1}^Y [x_{y1} - x_{y2}] [x'_{y1} - x'_{y2}] + \frac{1}{Y} \sum_{y=1}^Y [x_{y2} - x_{y3}] [x'_{y2} - x'_{y3}] \right\}, \quad (3.4)$$

237 and

238
$$b = \frac{1}{2} \left\{ \frac{1}{Y} \sum_{y=1}^Y [x_{y1} - x_{y2}] [x'_{y2} - x'_{y3}] + \frac{1}{Y} \sum_{y=1}^Y [x_{y2} - x_{y3}] [x'_{y1} - x'_{y2}] \right\}. \quad (3.5)$$

239 The χ^2 test and Student's *t*-test, used to judge the significance of the interannual
 240 covariance of the predictable and unpredictable component, respectively, are
 241 documented in the Appendix of Ying et al. (2018; their Eqs. 10–14).

242 The interannual (co-)variance of the predictable (or slow) and residual predictable
 243 (or residual slow) components of EASMR are calculated by Eq. (3), using the
 244 monthly means of the EASMR and the residual EASMR (Section 2.2.1), respectively.
 245 An EOF analysis can then be applied to each covariance matrix to derive the
 246 dominant modes of the interannual variability of EASMR. For simplicity, the EOF
 247 modes derived from the predictable (or slow) and residual predictable (or residual
 248 slow) covariance matrix are denoted by P-EOF and RP-EOF, respectively. The
 249 detailed sequence of steps for deriving the P-EOF (the same as for RP-EOF, but using
 250 the residual EASMR) patterns are listed in the Appendix.

251 By mapping the EASMR (or residual EASMR) fields onto the corresponding
 252 P-EOF (or RP-EOF), their associated principal component (PC) time series can then
 253 be calculated. Similarly, the PC time series corresponding to the P-EOF and RP-EOF
 254 are referred to as the P-PC and RP-PC, respectively. In addition, the EOF and PC
 255 derived directly from the total EASMR (or residual EASMR) fields without the
 256 (co-)variance decomposition are denoted by T-EOF (or RT-EOF) and T-PC (or
 257 RT-PC), respectively.

258 2.2.3 Prediction and validation

259 Let $\hat{\mathbf{r}}_y$ denote the prediction of the EASMR seasonal mean field in year *y* based
 260 on a PC regression, which can be expressed as

261
$$\hat{\mathbf{r}}_y = \hat{p}_{1,y}\mathbf{e}_1 + \hat{p}_{2,y}\mathbf{e}_2 + \dots + \hat{p}_{J,y}\mathbf{e}_J, \quad (4)$$

262 where $\{\mathbf{e}_j, j = 1, \dots, J\}$ is a set of predictable EOF modes of the EASMR (or the
 263 DC/DV ENSO–AO–related EASMR, or the EASMR linearly independent to DC/DV
 264 ENSO–AO), $\hat{p}_{j,y}$ is the corresponding j th ($j = 1, \dots, J$) predicted PC time series in
 265 year y , which can be predicted by linear regression using selected predictors.

266 The fraction variance skill, which is expressed as the percentage of explained
 267 variance (Wilks 1995), is used for evaluating our PC regression scheme. The skill can
 268 be expressed as

269
$$\mathbf{FV} = 100 \left(1 - \frac{\sum_y \|\mathbf{r}_y - \hat{\mathbf{r}}_y\|^2}{\sum_y \|\mathbf{r}_y - \bar{\mathbf{r}}\|^2} \right), \quad (5)$$

270 where $\hat{\mathbf{r}}_y$ is calculated by Eq. (4), \mathbf{r}_y is the observed seasonal mean EASMR field
 271 (total seasonal mean EASMR) in year y , $\bar{\mathbf{r}}$ is the climatological field of \mathbf{r}_y , and
 272 $\|\ \|\$ is the Euclidean distance operator. The skill scores range from minus infinity to
 273 100 (perfect forecast). Negative values indicate that the forecast is less accurate than
 274 the climatology, and positive values more accurate.

275 To lessen the over-fitting problem, the cross-validation method used by Wang et
 276 al. (2015) is applied to evaluate our forecast scheme. The whole period (1979–2020)
 277 is partitioned into fourteen 3-year intervals. We leave the 3-year data in each interval
 278 (verification period) out progressively. Then, we construct the prediction equations
 279 using the remaining years (training period), and forecast the rainfall in the three target
 280 years. Here, the cross-validation is applied to estimate the connections between the
 281 PC predictands \hat{p}_j and their associated predictors, but not to the EOFs.

282 **2.2.4 Potential predictability**

283 A theoretical estimation for the seasonal potential predictability is expressed as
 284 the percentage between the interannual variance of the predictable component $V(\mu_y)$,

285 which is calculated by Eq. (3), and the interannual total variance $V(x_{yo})$, which is
 286 calculated directly from seasonal mean fields; that is,

$$287 \quad \text{PP} = 100 \frac{V(\mu_y)}{V(x_{yo})}. \quad (6)$$

288 The larger the potential predictability (ranging from 0 to 100), the more likely it is
 289 that the seasonal mean time series can be predicted.

290 Then, the cumulative variance percentage of the seasonal mean EASMR (total
 291 EASMR) explained by the leading j th ($j = 1, \dots, J$) P-PCs (or T-PCs or RP-PCs) in the
 292 total, predictable and unpredictable components can be expressed as

$$293 \quad \text{AEV}.t = 100 \frac{\sum_{j=1}^J V(p_{yo}(j))}{\sum_{n=1}^N V(r_{yo}(n))}, \quad (7)$$

$$294 \quad \text{AEV}.p = \frac{\sum_{j=1}^J [V(p_{yo}(j)) \times \text{PP}(p_{yo}(j))]}{\sum_{n=1}^N V(r_{yo}(n))}, \quad (8)$$

295 and

$$296 \quad \text{AEV}.u = \frac{\sum_{j=1}^J \{V(p_{yo}(j)) \times [100 - \text{PP}(p_{yo}(j))]\}}{\sum_{n=1}^N V(r_{yo}(n))}, \quad (9)$$

297 respectively, where $p_{yo}(j)$ denotes the j th ($j = 1, \dots, J$) seasonal mean EASMR
 298 P-PCs (or T-PCs or RP-PCs) and $r_{yo}(n)$ denotes the total seasonal mean EASMR in
 299 a specific location n ($n = 1, \dots, N$). The predictable-to-total variability PP is
 300 calculated by Eq. (6).

301 **3 Indices for the EASMR predictability related to DC/DV ENSO–AO**

302 **3.1 DC ENSO, DV ENSO and spring AO–related predictable modes**

303 The first three P-EOF modes of the EASMR (which explain 22%, 13% and 9% of

304 the interannual variance in the predictable component; Table 1) and their associated
305 SST correlation, or the 500 hPa slow covariance maps at a one-season-lead
306 [March–April–May (MAM)] are displayed in Fig. 1.

307 EASMR P-EOF1 has a generally north–south dipole structure, with wetter
308 conditions along the Yangtze–Huaihe River Valley to South Japan and drier conditions
309 over the western North Pacific around the Philippines (Fig. 1a). EASMR P-EOF3 is
310 characterized by wetter-than-normal conditions over southern China and the
311 Indochina Peninsula, and drier conditions in the north and south of southern China
312 (Fig. 1e). The one-season-lead (MAM) SST correlations associated with both
313 EASMR P-EOF1 (Fig. 1b) and EASMR P-EOF3 (Fig. 1f) show significant positive
314 values in the tropical Pacific Ocean, suggestive of possible influences from ENSO.
315 However, the maximum warming center associated with P-EOF1 is observed in the
316 equatorial eastern Pacific (EP; Fig. 1b), while it is in the central Pacific (CP; Fig. 1f)
317 for P-EOF3 of the EASMR. In addition, when examining the SST correlation maps
318 associated with P-PC1 and P-PC3 from the preceding winter to the following summer,
319 there is an apparent evolution in the tropical Pacific. From the preceding November to
320 June–July–August (JJA), the correlation between P-PC1 and EP ENSO is getting
321 weaker and vanishes in JJA (Fig. 2), while the correlation between P-PC3 and CP
322 ENSO becomes stronger (Fig. 3). Thus, EASMR P-EOF1 and P-EOF3 are closely
323 associated with DC EP ENSO and DV CP ENSO, respectively.

324 The spatial structure of EASMR P-EOF2 displays excessive rainfall over
325 southeastern China, the lower reaches of the Yangtze River valley and northeastern
326 China but a deficient rainfall center over the East China Sea, Indochina Peninsula and
327 east of the Philippines (Fig. 1c). The slow covariance of the one-season-lead (MAM)
328 500 hPa height field associated with EASMR P-EOF2 (Fig. 1d) represents an
329 AO/NAO-like zonal structure [e.g., Frederiksen and Zheng (2004, their Fig. 4); Zheng
330 et al. (2008, their Fig. 3), but in JJA], which is characterized by opposite anomalies
331 over Greenland and northern Europe. It indicates a strong relationship between
332 EASMR P-EOF2 and the spring AO/NAO slow variability.

333 **3.2 Selected indices for DC EP ENSO, DV CP ENSO and spring AO**

334 Based on the analyses above, the predictors for the dominant three EASMR
335 P-EOFs, which best represent the EASMR predictability in DC EP ENSO, DV CP
336 ENSO and spring AO variability, are selected using stepwise regression. To provide
337 flexibility, we put the m ($m = 1, \dots, 9$)-month(s)-lead (that is, from preceding autumn
338 to the following spring) mean values of the most commonly used climate indices as
339 candidate predictors.

340 For EASMR P-PC1, we consider the lagged SST anomalies over the Niño 1+2,
341 Niño 3, Niño 4 and Niño 3.4 regions as candidate predictors (Fig. 1b). In this case, we
342 use stepwise regression to select the winter [preceding November to March (NDJFM)]
343 Niño 1+2 index as the best predictor for EASMR P-PC1. This is because the
344 relationship between EASMR P-EOF1 and the extreme eastern tropical Pacific SST
345 (Niño 1+2) is rather stable from the preceding winter to the following summer, and
346 their correlations reach maximum values in NDJFM (Fig. 2). We also tried the DJF
347 Niño3.4 SST as in Wu et al. (2009a), where it is identified as a predictor for the
348 EASM index of Wang and Fan (1999) and best represents the DC ENSO variability.
349 However, the interannual variability in the predictable component [Eq. (3)] of
350 EASMR P-PC1 explained by the DJF Niño 3.4 SST (31%) is much lower than that
351 with the NDJFM Niño 1+2 SST (57%). Also, the predictable variability [Eq. (3)] of
352 the EASM index of Wang and Fan (1999) explained by the DJF Niño3.4 SST (38%) is
353 lower than that with the NDJFM Niño 1+2 SST (59%).

354 To predict the PC time series associated with EASMR P-PC3, we also take the
355 lagged SST anomalies over the Niño 1+2, Niño 3, Niño 4 and Niño 3.4 regions as
356 candidate predictors (Fig. 1f). The May Niño 4 index, which quantitatively measures
357 the development of CP ENSO, is selected as the best predictor of this mode. This is
358 because the correlations between EASMR P-EOF3 and the central tropical Pacific
359 SST (Niño 4) are largest in May (Fig. 3). The interannual variability in the predictable
360 component [Eq. (3)] of EASMR P-PC3 explained by the May Niño 4 SST is largest
361 (32%). We also tried the Niño3.4 SST difference between April–May (AM) and

362 February–March (FM) as in Wu et al. (2009a), in which it is suggested as the
363 predictor for the monsoon index of Wang and Fan (1999) that best represents the DV
364 ENSO variability. However, the temporal correlation between EASMR P-PC3 and the
365 AM minus FM Niño3.4 SST is statistically insignificant (0.10). This is expected and
366 generally consistent with Wang et al. (2008b); in particular, the Wang and Fan (1999)
367 monsoon index is mostly related to EASMR P-PC1 (with an explained predictable
368 variance of 55%), but unrelated to EASMR P-PC3 (with an explained predictable
369 variance of almost zero).

370 The lagged NAO index of Barnston and Livezey (1987) and Li and Wang (2003),
371 as well as the lagged AO index (Higgins et al. 2002), are considered as candidate
372 predictors of EASMR P-PC2 (Fig. 1d). Our method selects the spring (AM) AO,
373 which explains the largest interannual variability in the predictable component [Eq.
374 (3)] of EASMR P-PC2 (28%), as the best representative indicator. Frederiksen and
375 Zheng (2004) suggested that the AO is potentially more predictable than the NAO, as
376 the latter is also strongly associated with the Greenland blocking, which is related to
377 intraseasonal variability.

378 As the NDJFM Niño 1+2 SST, May Niño 4 SST and AM AO explain the largest
379 variability in the predictable component of the corresponding EASMR P-PCs, they
380 are selected as indices to quantitatively measure the predictable EASMR signals
381 related to the DC EP ENSO, DV CP ENSO and spring AO variabilities, respectively.
382 The correlations among the above three indices are statistically insignificant at the
383 95% confidence level. Moreover, the SST correlations associated with the leading
384 P-EOFs display notable loadings in many other oceans, raising the question of which
385 among these provides the most important additional source of EASMR predictability
386 besides DC/DV ENSO and the spring AO? This is further explored next, in Section 4.

387 **4 Predictable sources additional to DC/DV ENSO and the spring AO:**

388 **Residual predictable modes**

389 4.1 RP-EOF1

390 EASMR RP-EOF1, with an explained variance of 31% in the residual predictable
391 component (Table 1), is shown in Fig. 4a. This phase is characterized by wetter
392 conditions over the East China Sea and southern Japan, and drier conditions over the
393 southeast of China and east of the Philippines. EASMR RP-EOF1 is significantly
394 related to an anomalous cyclone around the East China Sea (vectors in Figs. 4c and d).
395 In response, the significant moisture convergence anomaly over the East China Sea
396 (Fig. 4c) is responsible for this predictable rainfall pattern.

397 When examining the SST correlations associated with EASMR RP-EOF1 from
398 the preceding March to May (Figs. 4e–g), the most noticeable features are the
399 significant positive anomalies in the southern Atlantic Ocean off the
400 Argentina–Uruguay coast (60° – 30° W, 30° – 45° S) during March–April (MA; Figs. 4f
401 and g), and the negative values in the western North Pacific Ocean (0° – 20° N,
402 120° – 150° E) during AM (Figs. 4e and f). In particular, the interannual variability in
403 the predictable component [Eq. (3)] of EASMR RP-PC1 (Fig. 4b) explained by the
404 detrended southern Atlantic SST index in MA and the detrended western North
405 Pacific SST index in AM [with the DC/DV ENSO and spring AO signals removed for
406 both indices, using linear regression (as in Section 2.2.1 but for the climate index)] are
407 55% and 34%, respectively, significant at the 99.9% confidence level.

408 A previous study by Yim et al. (2016) also suggested a close relationship between
409 the spring equatorial western Pacific SST and the EOF1 of July–August rainfall in
410 extratropical East Asia (see their Fig. 2a). Besides, their SST correlation map (see
411 their Fig. 3a) associated with the rainfall EOF1 shows significant values in the
412 southern Atlantic. However, their rainfall pattern also has an impact from the DC
413 ENSO; in particular, the lagged SST correlation map associated with their rainfall
414 EOF1 has a clear linkage with the Niño 1+2 SST (see their Fig. 3a), which has been
415 identified as the precursor of DC ENSO. Moreover, their rainfall EOF1 (see their Fig.
416 2a) has significant loadings in the Yangtze–Huaihe River region, which is like our DC
417 ENSO–related P-EOF1 mode (Fig. 1a), while this is not the case for RP-EOF1 (Fig.

418 4a). Therefore, the EASMR RP-EOF1 in this work emphasizes the independence of
419 the influences of the spring western North Pacific and southern Atlantic SST on
420 EASMR from those of DC/DV ENSO.

421 **4.2 RP-EOF2**

422 The spatial structure of EASMR RP-EOF2 (with an explained variance of 25%;
423 Table 1) is shown in Fig. 5a. In the phase shown here, there are positive loadings
424 corresponding to wet conditions over southeastern China and south of Japan, and
425 negative loadings corresponding to drier-than-normal conditions over northeastern
426 China and the Japan Sea (Fig. 5a). From Fig. 5d, there is an anomalous cyclone
427 centered over southeastern China and the south of Japan (vectors in Fig. 5d) and an
428 anomalous high centered over northeastern China (vectors in Figs. 5d and e). As a
429 result, anomalous moisture convergence is situated in southeastern China, and
430 moisture divergence around northeastern China (Fig. 5d), causing this predictable
431 rainfall pattern over East Asia.

432 During the period 1979–2019, there is a prolonged positive trend, which is
433 statistically significant at the 99.9 % confidence level, in the PC time series associated
434 with EASMR RP-EOF2 (Fig. 5b). In fact, the predictable variance [Eq. (3)] of
435 EASMR RP-PC2 (Fig. 5b) explained by the linear trend series (consecutive years
436 from 1 to 41) is 60%. Consistent with this, the one-season-lead (MAM) SST
437 correlations associated with this “trend mode” (Fig. 5c) displays large positive
438 anomalies over most of the domain, with the largest loadings over the northern
439 Atlantic and northwestern Pacific, indicating global SST warming associated with this
440 phase of the “trend mode”. We also investigated the detrended SST correlation map
441 associated with the detrended EASMR RP-EOF2. However, the significant centers
442 over the northern Atlantic, northwestern Pacific and Indian Ocean that can be seen in
443 Fig. 5c no longer exist. Thus, besides the trend, they could not provide additional
444 sources of predictability.

445 A previous study by Wang et al. (2015) also identified an Asian summer monsoon

446 rainfall pattern (EOF4 in their Fig. 2d) associated with the trend. However, their
447 rainfall pattern also has an impact from the Indo-Pacific warm pool SST (see their Fig.
448 4d), while this is not the case for our RP-EOF2. In particular, the correlation between
449 the PC associated with their EOF4 and the Indo-Pacific warm pool SST (see their Fig.
450 4d) is significant (larger than 0.68), while the correlation for our EASMR RP-PC2 is
451 statistically insignificant at the 95% confidence level.

452 **4.3 RP-EOF3**

453 Figure 6 shows the spatial and temporal variations of EASMR RP-EOF3, as well
454 as its associated SST anomalies in MAM and the simultaneous atmospheric
455 circulation correlation patterns. The explained variance of this mode is 18% (Table 1).
456 This phase is characterized by deficient rainfall centers over the Indochina Peninsula,
457 east of the Philippines and around the east of Taiwan but excessive rainfall over
458 northeastern China, southern Japan and the east of Hainan Province (Fig. 6a).
459 Associated with EASMR RP-EOF3 is an anomalous cyclonic center over northeastern
460 China and an anomalous anticyclonic circulation center over east of the Philippines
461 (vectors in Figs. 6c and d). Corresponding to these anomalous moisture transport
462 circulations, moisture convergence is located in southern Japan and northeastern
463 China, and moisture divergence in southeastern China and east of the Philippines (Fig.
464 6c), consistent with the rainfall pattern in this area.

465 The correlations of the preceding SST associated with EASMR RP-EOF3 (Figs.
466 6e–g) display notable warming conditions over the tropical southern Atlantic
467 (30°W – 10°E , 0° – 20°S), with the maxima in May (Fig. 6e). Also, it shows an apparent
468 east–west dipole SST pattern in the southern Indian Ocean during March (Fig. 6g),
469 with significant SST differences between the east (80° – 140°E , 15° – 65°S) and the
470 west (45° – 80°E , 30° – 55°S). In particular, the predictable variability [Eq. (3)] of
471 EASMR RP-PC3 (Fig. 6b) explained by the May detrended tropical southern Atlantic
472 SST index and the March southern Indian Ocean SST index (with the DC/DV ENSO
473 and spring AO signals removed in both indices) are 48% and 36%, respectively,

474 significant at the 99.9% confidence level. This indicates that EASMR RP-EOF3 has a
475 combined impact from the variability of the tropical southern Atlantic SST and
476 southern Indian SST during spring.

477 Based on both observations and model-based experiments, Jin and Huo (2018)
478 found that the tropical Atlantic (20°N–20°S, 10°E–80°W) SST warming from the
479 previous boreal spring can enhance an anomalous anticyclone over the northwestern
480 Pacific and further impacts the EASMR. Although the tropical southern Atlantic
481 (0°–20°S, 10°E–30°W) is largely covered by the tropical Atlantic, the influence of
482 their tropical Atlantic SST on the EASMR (see their Fig. 3d) differs from that seen in
483 our RP-EOF3 (Fig. 6a) over the areas from Hainan Island to the Philippines. This may
484 be partly because of the removal of the ENSO signal in our work, which was not the
485 case for their tropical Atlantic SST, which is significantly related to the DV ENSO
486 variability (see their Fig. 8). In fact, the temporal correlation between the May Niño 4
487 SST and their May detrended tropical Atlantic SST is -0.34 , significant at the 95%
488 confidence level.

489 **4.4 RP-EOF4**

490 The spatial structure of EASMR RP-EOF4 (with an explained variance of 14%;
491 Table 1) is presented in Fig. 7a. In this phase, the most notable features in the
492 precipitation pattern are the drier conditions in southeastern China and the wetter
493 conditions around Taiwan and the Philippines. From the vectors in Figs. 7d and e, a
494 cyclonic anomaly center around Mongolia and an anticyclonic center in the
495 northwestern Pacific can be seen. Consistent with this circulation anomaly, there is
496 anomalous moisture divergence in southeastern China and moisture convergence in
497 the east of Taiwan (Fig. 7d), causing this predictable rainfall pattern over East Asia.

498 A notable characteristic in the one-season-lead (MAM) SST correlation map is
499 the positive correlation values over the broad Arctic Ocean (Fig. 7c), covering
500 longitudes of 20°–150°E and latitudes of 70°–90°N. In particular, the variance in the
501 predictable component of EASMR RP-PC4 [Eq. (3)] explained by the Arctic Ocean

502 SST index (with the DC/DV ENSO and spring AO signals removed) in MAM is 50%,
503 significant at the 99.9% confidence level. This indicates that the Arctic Ocean SST is
504 an important source of predictability for EASMR RP-EOF4.

505 Wu et al. (2009b) investigated the association between the spring Arctic sea-ice
506 concentration and the summer rainfall in China, and found a close positive
507 relationship between the former and the latter in southeastern China. Guo et al. (2014)
508 further indicated that the SST changes in the North Pacific play a mediating role for
509 this connection between the spring Arctic sea ice and the EASM. As the Arctic sea ice
510 is negatively correlated with the Arctic Ocean SST, these results are generally
511 consistent with ours above. However, using the MAM Arctic sea ice as a predictor for
512 EASMR RP-PC4 instead of the Arctic Ocean SST, the explained variance in the
513 predictable component is lower (20%).

514 **5. Predictability of EASMR from DC/DV ENSO, the spring AO and** 515 **additional sources**

516 To further understand the relative importance of the EASMR predictability
517 arising from DC/DV ENSO–AO and the additional sources, we construct a PC
518 regression scheme [see Section 2.2.3; Eq. (4)] for the seasonal forecasting of EASMR
519 at each grid point using different sets of predictors and predictands.

520 Scheme-*A* is designed to study the EASMR predictability arising from DC/DV
521 ENSO and the spring AO. It uses a PC regression scheme [Eq. (4)], employing the
522 NDJFM Niño 1+2 SST, May Niño 4 SST and AM AO as predictors (top three rows in
523 Table 2; Section 3), and the dominant predictable PCs derived from the DC/DV
524 ENSO–AO–related EASMR as predictands.

525 Scheme-*B* is designed to study the predictability arising from those sources
526 additional to DC/DV ENSO and the spring AO. In this PC regression scheme [Eq. (4)],
527 the predictors are the identified predictable sources of the dominant four RP-EOFs –
528 the AM detrended western North Pacific SST, the MA detrended southern Atlantic

529 SST, the linear trend, the May detrended tropical southern Atlantic SST, the March
530 southern Indian SST, and the MAM Arctic Ocean SST (bottom six rows in Table 2;
531 Section 4); and the predictands are the predictable PCs derived from the EASMR that
532 is linearly correlated to the predictors of the leading four RP-EOFs. Note that the
533 DC/DV ENSO and spring AO signals are removed from the time series of this set of
534 predictors, using linear regression (as in Section 2.2.1, but for climate predictors).

535 Scheme-*AB* is a combination of Scheme-*A* and Scheme-*B*. In particular, the
536 predictands of Scheme-*A* and Scheme-*B* are statistically independent. Therefore, the
537 variabilities predicted by Scheme-*A* and Scheme-*B* are statistically independent.

538 Generally, the cross-validated fraction variance skill [Eq. (5)] of the seasonal
539 mean EASMR can reach an average of 11% for the PC regression Scheme-*A*, and
540 15% for Scheme-*B*, over East Asia (Table 3). This suggests that the predictors
541 additional to DC/DV ENSO–AO are of equal importance to those sourced from
542 DC/DV ENSO–AO. Furthermore, comparing the cross-validated fraction variance
543 skill scores over land and ocean between the two schemes (Table 3), considerably
544 larger skill is achieved over land areas in Scheme-*B* (15%) than Scheme-*A* (8%),
545 while the skill scores of the two schemes are equivalent over ocean areas (13% for
546 Scheme-*A* and 15% for Scheme-*B*). This indicates that the predictability due to
547 sources additional to DC/DV ENSO–AO is important, especially for land areas. The
548 spatial distributions of the cross-validated fraction variance skill of Scheme-*A* (Fig. 8c)
549 and Scheme-*B* (Fig. 8d) display large differences, especially over land. In particular,
550 Scheme-*A* has its largest skill (larger than 20%) in the northwestern Pacific Ocean
551 around the Philippines (Fig. 8c), while the maximum centers (larger than 20%) for
552 Scheme-*B* are in the land areas of southeastern and northeastern China and the
553 Indochina peninsula, as well as the ocean areas of the northwestern Pacific and the
554 East China Sea (Fig. 8d).

555 For the PC regression Scheme-*AB*, which considers all the identified predictors in
556 Table 2 (DC/DV ENSO, the spring AO and additional sources), the cross-validated
557 fraction variance skill [Table 3; Eq. (5)] of the total seasonal mean EASMR reaches
558 an average of 26% over East Asia, comparable to that in the observation (28%). This

559 is also comparable to the EASMR potential predictability (31%; theoretical estimate
560 of predictable-to-total variance in Section 2.2.4), and more details about the potential
561 predictability are given below, in Section 6.3.1. Furthermore, when examining the
562 spatial pattern of the cross-validated fraction variance skill for the PC regression
563 Scheme-*AB* (Fig. 8b), it generally has three maximum centers. One is located along
564 the Mei-yu rain belt, which stretches from southeastern China to south of Japan; one
565 is situated over the northwestern Pacific around the Philippines; and the other is
566 located over northeastern China. The largest loading centers are consistent with those
567 seen in the observations (Fig. 8a); however, the overall values are slightly lower, as
568 expected.

569 **6 Discussion and Conclusions**

570 **6.1 Methods-related discussion**

571 In this study, the EOFs and their corresponding PCs are not derived from the
572 covariance matrices of the EASMR total seasonal mean fields, but from the
573 covariance matrices of the predictable (or slow) component of the EASMR seasonal
574 mean fields, using Eq. (3). This is because, in general, the EOFs and their associated
575 PC time series in the predictable component are potentially more predictable on
576 seasonal or longer time scales (Table 1), and thus maximize the predictive
577 characteristics. More details are provided as follows:

578 (1) In section 4, if the total covariance matrix of the seasonal mean of the residual
579 EASMR is applied to derive the RT-EOF modes, the RT-EOF modes have some
580 similarities in the spatial distributions of the dominant four RP-EOF modes, but they
581 also have characteristics of the corresponding residual intraseasonal (or unpredictable)
582 component. Consequently, the hybrid characteristics in the total seasonal mean fields
583 may make it harder to elucidate the predictable signals from SST and atmospheric
584 circulations, or even miss them.

585 (2) In section 5, if a PC regression scheme is built by predicting the dominant
586 four total PCs, the cross-validated fraction variance skill [Eq. (5)] of the total seasonal
587 mean EASMR in the PC regression Scheme-*AB* is 17% on average, which is lower
588 than that using predictable EOFs (average of 26%; Fig. 8b). Although the leading
589 total PCs have a higher explained variance of the interannual variability in the total
590 component than the leading predictable PCs, the unpredictable noise of the EASMR
591 plays a role in decreasing the predictability (Table 1).

592 In addition, the main purpose of this work is to better understand the critical
593 predictable sources of EASMR, especially those in addition to the well-known climate
594 precursor signals of DC/DV ENSO–AO. Thus, the EASMR component forced by
595 DC/DV ENSO–AO is separated in this study by a pointwise linear regression with the
596 three indices – the preceding NDJFM Niño 1+2 SST, AM AO, and May Niño 4 SST.
597 It is demonstrated that there are no DC ENSO, spring AO and DV ENSO signals in
598 the dominant four EASMR RP-EOFs, which indicates that the separation is
599 successful.

600 **6.2 Robustness across datasets**

601 Our analysis above is based on the monthly precipitation of the GPCP datasets.
602 For comparison, we further apply the PC regression scheme-*AB*, using the predictors
603 in Table 2 and the predictands based on different precipitation datasets of CMAP and
604 PREC. The cross-validated fraction variance skill [Eq. (5)] of the total seasonal mean
605 EASMR reaches an average of 25% for the CMAP and 27% for the PREC datasets.
606 This is comparable to that for the GPCP prediction scheme (26%), as well as for
607 CMAP and PREC observations (28% and 30%). Consistent with this, the spatial
608 distributions of the fraction variance skills of the total seasonal mean EASMR from
609 the observations (Fig. 8a and Figs. S1a and S1c) and the cross-validated PC prediction
610 scheme-*AB* (Fig. 8b and Figs. S1b and S1d) show quite similar maximum loadings
611 among the datasets of GPCP, CMAP and PREC. This indicates that the most
612 significant sources of predictability identified for EASMR (Table 2) are generally

613 robust across datasets.

614 It is of interest to predict the EASMR that occurred in 2020 using the above three
615 datasets, because eastern China experienced an extraordinarily wet summer that year
616 (bottom row of Fig. S2), without significant DC/DV ENSO and AO signals in
617 preceding seasons. Using the identified predictors in Table 2, we construct a PC
618 regression Scheme-*AB* for the seasonal forecasting of the 2020 summer rainfall. The
619 independent period of 1979–2019 is used as the training period. The predicted rainfall
620 anomalies are presented in the top row of Fig. S2. Compared to the observation,
621 similar spatial distributions but lower variability can be seen in the predicted rainfall
622 for all three datasets. In fact, the most notable features in the SST anomalies from
623 March to May of 2020 include an anomalous southern Indian dipole SST pattern with
624 maxima in March, a warmer-than-normal tropical southern Atlantic SST in May, a
625 SST anomaly center over the southern Atlantic Ocean with maxima in MA,
626 anomalous conditions over the Arctic Ocean at longitudes of 20°–150°E during MAM,
627 and anomalous higher-than-normal SST conditions over the northern Atlantic and
628 northwestern Pacific Oceans in MAM, which indicates potential influences from the
629 trend. Recall that these have been identified as the most important EASMR
630 predictable sources in addition to DC/DV ENSO and the spring AO. This case study
631 also indicates that the predictors identified here are possible candidates in providing
632 skillful and generally robust EASMR forecasting.

633 **6.3 Discussion on the EASMR predictability and its main sources**

634 *6.3.1 How much of the EASMR predictability is due to DC/DV ENSO–AO and any of*
635 *the additional sources identified?*

636 In Section 5, the relative importance of the identified predictors to the seasonal
637 forecasting of EASMR was evaluated in terms of the fraction variance skill in a
638 cross-validated PC regression scheme. Generally, the cross-validated variance
639 percentage of the total seasonal mean EASMR explained by the predictors listed in

640 Table 2 is 26%. Although 26% of the total variance may seem low, this is comparable
641 to the cumulative variance percentage of the total seasonal mean EASMR explained
642 by the leading six EASMR P-PCs in the predictable component (31%; Table 1). The
643 first six EASMR P-PCs have the best potential predictabilities and explain most of the
644 variability in the predictable component, and thus the cumulative variance percentage
645 of the total seasonal mean EASMR explained by the leading six EASMR P-PCs in the
646 predictable component could be considered as an approximate estimation of the
647 EASMR potential predictability (predictable-to-total variance in Section 2.2.4).
648 Therefore, the identified predictors in this work provide the most important source of
649 EASMR predictability, which together comprise more than 80% of the potential
650 predictability.

651 *6.3.2 What are the most important additional sources of EASMR predictability besides*
652 *DC/DV ENSO and the spring AO?*

653 In this work, the sources of EASMR predictability are investigated from two
654 statistically independent components. One is related to DC/DV ENSO–AO (Section
655 3), and the other additional to DC/DV ENSO–AO (Section 4). A summary of the
656 identified predictors is provided in Table 2. However, it should be noted that, besides
657 the key SST areas as in Table 2, significant correlations in preceding SST maps
658 associated with the EASMR P-EOFs can also be seen in some oceans. For instance,
659 there are notable loadings in the tropical Indian Ocean associated with P-EOF1 (Figs.
660 1b and 2). However, the tropical Indian SST cannot provide statistically significant
661 additional prediction skill for P-EOF1 with respect to DC ENSO, and it does not
662 appear in the SST correlations with the dominant four RP-EOFs. This is probably due
663 to the fact that the influences from the tropical Indian Ocean and DC ENSO on the
664 EASMR predictable signals are closely coupled. As suggested by Xie et al. (2009),
665 there is a lingering effect of DC El Niño on EASMR, while the El Niño–induced
666 tropical Indian Ocean warming following the mature stage of El Niño behaves as a
667 capacitor in connecting the atmosphere over the Indian Ocean to the western Pacific.

668 Therefore, to avoid the problem of a mixed predictable EASMR source, the RP-EOFs
669 in this work are derived by separating the DC/DV ENSO–AO-related variabilities,
670 and thus emphasize the most important predictable sources of EASMR arising in
671 addition to DC/DV ENSO–AO.

672 Besides the SST predictors of the RP-EOFs during boreal spring, we also try to
673 identify the additional predictors from the SST anomalies in the prior winter and
674 autumn seasons, but find that they add barely any additional prediction skill. However,
675 there may be additional sources of predictability that stem from the thermodynamic
676 processes of the Qinghai–Tibet Plateau (Xiao and Duan 2016) and snow cover over
677 northern Eurasia (Yim et al. 2010). Moreover, it should be noted that the precipitation
678 variability in East Asia has large regional differences, with much smaller loadings
679 over the area north of 35°N than the south. Thus, in the future, we plan to partition
680 East Asia into several subregions and apply the method focusing on a smaller
681 objective area in order to better understand its predictable sources and to enhance its
682 prediction skill. These are all interesting issues to be explored in future work.

683 *6.3.3 Predictability arising from the predictors one month ahead*

684 The EASMR predictors identified here (Table 2) are those before June, i.e., at
685 zero-month lead. For practical applications, it is important to predict the EASMR at a
686 one-month lead (i.e., before May). In fact, four of our nine identified predictors,
687 including DC ENSO, the southern Atlantic SST, trend, and southern Indian SST, are
688 defined before May. The rest, including the spring AO, DV ENSO, western North
689 Pacific SST, tropical southern Atlantic SST, and Arctic Ocean SST, also have
690 significant correlations with the EASMR before May. Thus, we construct a PC
691 regression scheme-*AB* using the predictors at a one-month lead, in which the indices
692 of the AO, Niño4 SST, detrended western North Pacific SST, and detrended tropical
693 southern Atlantic SST are constructed with values in April, and the Arctic Ocean SST
694 index is built with values in MA. On average, the cross-validated fraction variance
695 skill [Eq. (5)] of the total seasonal mean EASMR reaches 23% for the one-month-lead

696 predictors, which is slightly lower than that for the zero-month lead (26%).
697 Consistently, compared to Fig. 8b, quite similar but slightly lower loadings are seen in
698 their spatial distributions (Fig. S3). This indicates the possibility for a skillful EASMR
699 seasonal forecast using the predictors in Table 2 but at a one-month lead time.

700 As indicated above, the MA southern Atlantic and March southern Indian SST
701 predictors are particularly important because their best correlations with EASMR
702 appear at the one-month lead. However, the dynamical mechanisms responsible for
703 the impact of the above two predictors on EASMR have not been fully disentangled.
704 To aid a better physical understanding of these two predictors, we further examine
705 their corresponding JJA precipitation, and SST and atmospheric circulations during
706 MAM and JJA. In spring, MA southern Atlantic warming is associated with an
707 anomalous anticyclone in the lower troposphere of the southern Atlantic and
708 strengthened easterly trade winds through the tropical Atlantic to the tropical EP (Fig.
709 S4c). It is followed, during the subsequent summer, by enhanced Walker circulation
710 (Fig. S4f). In particular, there is anomalous low-level cyclonic (Fig. S4e) and
711 anomalous high-level anticyclonic (Fig. S4d) circulation east of the Philippines over
712 the western North Pacific. This anomalous low-level cyclone covers the areas of East
713 China Sea and southern Japan (Fig. S4e) and enhances the rainfall there (Fig. S4a).
714 Meanwhile, an anomalous low-level anticyclone over Mongolia and northeastern
715 China occurs (Fig. S4e) and depresses the rainfall there (Fig. S4a). Associated with
716 the March southern Indian SST dipole, the SST correlation pattern in the subsequent
717 summer (Fig. S5d) is close to the type-4 ENSO pattern of Johnson (2013), with
718 significant warming loadings around the Maritime Continent between the latitudes of
719 10°N and 10°S and the longitudes of 100° and 160°E (Fig. S5d), which is consistent
720 with Zhou and Zhang (2021). Meanwhile, the low-level anticyclone in the western
721 North Pacific enhances (Fig. S5e) and the anomalous southerlies bring moisture from
722 the ocean to northern East Asia to cause wetter conditions there (Fig. S5a). We have
723 briefly discussed here the possible physical linkages between the EASMR and SST in
724 the southern Atlantic and southern Indian oceans during early spring. However,
725 coupled model experiments are required in future work to further understand and

726 interpret the underlying physical processes involved.

727 **6.4 Summary**

728 The main objective of this study was to understand the main sources of
729 predictability for the EASMR in the period 1979–2020, especially those in addition to
730 DC/DV ENSO and the spring AO. For this purpose, the dominant residual predictable
731 (slow) EASMR patterns that are linearly independent of DC ENSO, DV ENSO and
732 the spring AO were studied, using a (co-)variance decomposition method. Importantly,
733 with a (co-)variance decomposition method that allows us to separate the potentially
734 predictable (slow) component from the unpredictable noise (intraseasonal), we could
735 focus on the more predictable signals of the EASMR, as well as maximize the
736 predictive features of the precursor-rainfall relationship (details in Section 6.1). Also,
737 the most significant sources of predictability identified for EASMR were found to be
738 generally robust across the GPCP, CMAP and PREC precipitation datasets (details in
739 Section 6.2). The main results can be summarized as follows:

740 *(1) Predictable sources related to DC/DV ENSO and the spring AO*

741 The indices that best represent the EASMR predictability related to the DC
742 ENSO, spring AO and DV ENSO are selected from the most commonly used indices
743 from a predictability perspective. In particular, the leading three predictable EASMR
744 modes closely linked to the DC ENSO, spring AO and DV ENSO, respectively, are
745 identified as a first step. On this basis, the preceding NDJFM Niño 1+2 SST, AM AO
746 and May Niño 4 SST indices, which best represent the EASMR predictability related
747 to the DC ENSO, spring AO and DV ENSO, respectively, are chosen as those
748 explaining the largest variability in the predictable component.

749 *(2) Predictable sources in addition to DC/DV ENSO and the spring AO*

750 The dominant four residual predictable EASMR modes that are linearly
751 independent of ENSO in its DC and DV phases, as well as the spring AO, are closely
752 related to the SST anomalies in the southern Atlantic Ocean, western North Pacific
753 Ocean, tropical southern Atlantic Ocean, southern Indian Ocean and Arctic Ocean

754 during boreal springtime, as well as the linear trend. Thus, these are the most
755 important additional sources of EASMR predictability besides DC/DV ENSO and the
756 spring AO.

757 *(3) Relative importance of DC/DV ENSO–AO predictors and additional sources*

758 A PC regression scheme using predictable PCs as predictands is applied to
759 evaluate the EASMR predictability arising from DC/DV ENSO–AO and form
760 additional sources. It is found that the cross-validated fraction variance skill of the
761 total seasonal mean EASMR is 11% (8%–land; 13%–ocean) for the former, and 15%
762 (15%–land; 15%–ocean) for the latter, with a total of 26% that comprises more than
763 80% of the EASMR potential predictability. Thus, the identified predictors from
764 DC/DV ENSO–AO and the additional sources (Table 2) are potential indicators
765 dominating the EASMR predictability. Also, the considerable skill stemming from the
766 predictors in addition to DC/DV ENSO and the spring AO indicates that they are
767 worthy of attention in the seasonal forecasting of EASMR, especially for land areas –
768 the most important but also the most complex and difficult areas of East Asia with
769 respect to climate prediction.

770 In particular, we emphasize the importance of the March–April southern Atlantic
771 SST and the March southern Indian SST dipole for EASMR seasonal forecasting, as
772 their best correlations with EASMR appear at the one-month lead (i.e., before May).
773 Furthermore, we indicate that our identified predictors in Table 2 at the zero-month
774 lead (i.e., before June) also have the potential to provide skillful EASMR seasonal
775 forecasts at a one-month lead time, which is hugely important for operational seasonal
776 forecasting.

777 ***Acknowledgments.*** This work was supported by the National Key R&D Program of
778 China (2020YFA0608904) and the National Natural Science Foundation of China
779 (41991284).

780

Appendix

781

782

783 The steps in deriving the slow or predictable EOF patterns are:

784 (1) Derive the eigenvalues and eigenmodes of the total covariance matrix of the
785 seasonal mean rainfall using an EOF analysis.

786 (2) Project the monthly rainfall anomalies onto the obtained leading $Y - I$ (Y is
787 the total number of years) eigenmodes (EOF modes) to form the $Y - I$ truncated
788 monthly PC time series.

789 (3) Estimate the $(Y - 1) \times (Y - 1)$ covariance matrix of the intraseasonal
790 component for each pair of the $Y - I$ truncated monthly PC time series using Eq. (16)
791 of Zheng and Frederiksen (2004).

792 (4) The symmetric matrix from (3), above, is then pre-multiplied by the matrix of
793 the leading $Y - I$ EOF modes and post-multiplied by its transpose to form the full, or
794 raw, intraseasonal covariance matrix.

795 (5) If the r th diagonal element of the raw intraseasonal covariance matrix is
796 greater than its corresponding total variance, then the r th row and the r th column of
797 the raw intraseasonal covariance matrix are replaced by r th row and the r th column of
798 the total covariance matrix. This adjusted covariance matrix is the estimated
799 intraseasonal covariance matrix.

800 6. The slow covariance matrix is the difference between the total covariance
801 matrix and the estimated intraseasonal covariance matrix.

802 7. An EOF analysis is then applied to the slow covariance matrix to obtain the
803 corresponding patterns.

804

805 **References**

806

807 Adler RF, Huffman GJ, Chang A, Ferraro R, Xie PP, Janowiak J, Rudolf B, Schneider
808 U, Curtis S, Bolvin D, Gruber A, Susskind J, Arkin P, Nelkin E (2003) The
809 version-2 Global Precipitation Climatology Project (GPCP) monthly precipitation
810 analysis (1979–present). *J Hydrometeor* 4: 1147–1167

811 Barnston AG, Livezey RE (1987) Classification, seasonality and persistence of
812 low-frequency atmospheric circulation patterns. *Mon Wea Rev* 115: 1083–1126

813 Chen M, Xie P, Janowiak JE, Arkin PA (2002) Global land precipitation: A 50-yr
814 monthly analysis based on gauge observations. *J Hydrometeor* 3: 249–266

815 Ding Y, Chan JCL (2005) The East Asian summer monsoon: An overview. *Meteor
816 Atmos Phys* 89: 117–142

817 Fan K, Liu Y, Chen H (2012) Improving the prediction of the East Asian summer
818 monsoon: New approaches. *Wea Forecasting* 27: 1017–1030

819 Frederiksen CS, Zheng X (2004) Variability of seasonal-mean fields arising from
820 intraseasonal variability: Part2, application to NH winter circulations. *Clim Dyn*
821 23:193–206

822 Frederiksen CS, Zheng X, Grainger S (2014) Teleconnections and predictive
823 characteristics of Australian seasonal rainfall. *Clim Dyn* 43:1381–1408

824 Grainger S, Frederiksen CS, Zheng X (2017) Projections of Southern Hemisphere
825 atmospheric circulation interannual variability. *Clim Dyn* 48:1187–1211

826 Guan Z, Yamagata T (2003) The unusual summer of 1994 in East Asia: IOD
827 teleconnections. *Geophys Res Lett* 30: 1544

828 Guo D, Gao Y, Bethke I, Gong D, Johannessen OM, Wang H (2014) Mechanism on
829 how the spring Arctic sea ice impacts the East Asian summer monsoon. *Theor
830 Appl Climatol* 115: 107–119

831 He S, Gao Y, Li F, Wang H, He Y (2017) Impact of Arctic Oscillation on the East
832 Asian climate: A review. *Earth-Science Reviews* 164: 48–62

833 Higgins RW, Leetmaa A, Kousky VE (2002) Relationships between climate
834 variability and winter temperature extremes in the United States. *J Clim* 15:
835 1555–1572

836 Johnson NC (2013) How many ENSO flavors can we distinguish? *J Clim* 26:
837 4816–4827

838 Jin D, Huo L (2018) Influence of tropical Atlantic sea surface temperature anomalies
839 on the East Asian summer monsoon. *Q J R Meteorol Soc* 144: 1490–1500

840 Kalnay E, Kanamitsu M, Kistler R, Collins W, Deaven D, Gandin L, Iredell M, Saha
841 S, White G, Woollen J, Zhu Y, Leetmaa A, Reynolds R, Chelliah M, Ebisuzaki W,
842 Higgins W, Janowiak J, Mo KC, Ropelewski C, Wang J, Jenne R, Joseph D (1996)
843 The NCEP/NCAR 40-year reanalysis project. *Bull Am Meteorol Soc* 77:
844 431–471

845 Lee DY, Ahn JB, Yoo JH (2015) Enhancement of seasonal prediction of East Asian
846 summer rainfall related to western tropical Pacific convection. *Clim Dyn* 45:
847 1025–1042

848 Li C, Lu R, Dunstone N, Scaife A, Bett P, Zheng F (2021) The seasonal prediction of
849 the exceptional Yangtze River rainfall in summer 2020. *Adv Atmos Sci* 38:
850 2055–2066

851 Li J, Zeng Q (2002) A unified monsoon index. *Geophys Res Lett* 29: 1274

852 Li J, Wang J (2003) A new North Atlantic Oscillation index and its variability. *Adv*
853 *Atmos Sci* 20: 661–676

854 Li S, Lu J, Huang G, Hu K (2008) Tropical Indian Ocean basin warming and East
855 Asian summer monsoon: A multiple AGCM study. *J Clim* 21: 6080–6088

856 Liu YY, Ke ZJ, Ding YH (2019) Predictability of East Asian summer monsoon in
857 seasonal climate forecast models. *Int J Climatol* 39: 5688–5701

858 Park CK, Schubert SD (1997) On the nature of the 1994 East Asian summer drought.
859 *J Clim* 10: 1056–1070

860 Rayner NA, Parker DE, Folland CK, Alexander LV, Horton EB, Rowell DP (2003)
861 Globally complete analyses of sea-surface temperature, sea-ice and marine air
862 temperature, 1871–2000. *J Geophys Res* 108:4407

- 863 Rong X, Zhang R, Li T (2010) Impacts of Atlantic sea surface temperature anomalies
864 on Indo-East Asian summer monsoon–ENSO relationship. *Chin Sci Bull* 55:
865 2458–2468
- 866 Takaya YH, Kosaka Y, Watanabe M, and Maeda SH (2021) Skillful predictions of the
867 Asian summer monsoon one year ahead. *Nat Commun* 12: 2094
- 868 Trenberth KE (1997) The definition of El Niño. *Bull Amer Meteor Soc* 78:
869 2771–2777
- 870 Wang B, Fan Z (1999) Choice of South Asian summer monsoon indices. *Bull Amer*
871 *Meteor Soc* 80: 629–638
- 872 Wang B, Wu R, Fu X (2000) Pacific–East Asian teleconnection: How does ENSO
873 affect East Asian climate? *J Clim* 13: 1517–1536
- 874 Wang B, LinHo (2002) Rainy season of the Asian–Pacific summer monsoon. *J Clim*
875 15: 386–396
- 876 Wang B, Lee JY, Kang IS, Shukla J, Kug JS, Kumar A, Schemm J, Luo J, Yamagata T,
877 Park C (2008a) How accurately do coupled climate models predict the leading
878 modes of Asian–Australian monsoon interannual variability? *Clim Dyn* 30:
879 605–619
- 880 Wang B, Li J, Liu J, Chang CP, Ding Y, Wu G (2008b) How to measure the strength
881 of the East Asian summer monsoon. *J Clim* 21: 4449–4463
- 882 Wang B, Xiang B, Lee JY (2013) Subtropical high predictability establishes a
883 promising way for monsoon and tropical storm predictions. *Proc Natl Acad Sci*
884 110:2718–2722
- 885 Wang B, Lee JY, Xiang B (2015) Asian summer monsoon rainfall predictability: A
886 predictable mode analysis. *Clim Dyn* 44: 61–74
- 887 Wang C, Deser C, Yu JY, DiNezio P, Clement A (2016) El Niño and Southern
888 Oscillation (ENSO): A review. In: *Coral reefs of the eastern Pacific*, Glynn P,
889 Manzello D and Enochs I (eds), Springer Science Publisher, pp 85–106
- 890 Wilks DS (1995) *Statistical methods in the atmospheric sciences*. Academic Press,
891 Cambridge, pp 467
- 892 Wu B, Zhang R, Wang B, D’Arrigo R (2009b) On the association between spring

893 Arctic sea ice concentration and Chinese summer rainfall. *Geophys Res Lett* 36:
894 L09501

895 Wu Z, Wang B, Li J, Jin FF (2009a) An empirical seasonal prediction of the East
896 Asian summer monsoon using ENSO and NAO. *J Geophys Res* 114: D18120

897 Wu Z, Yu L (2016) Seasonal prediction of the East Asian summer monsoon with a
898 partial-least square model. *Clim Dyn* 46: 3067–3078

899 Xiao Z, Duan A (2016) Impacts of Tibetan Plateau snow cover on the interannual
900 variability of the East Asian summer monsoon. *J Clim* 29: 8495–8514

901 Xie P, Arkin PA (1997) Global precipitation: A 17-year monthly analysis based on
902 gauge observations, satellite estimates, and numerical model outputs. *Bull Amer*
903 *Meteor Soc* 78: 2539–2558

904 Xie SP, Hu K, Hafner J, Tokinaga H, Du Y, Huang G, Sampe T (2009) Indian Ocean
905 capacitor effect on Indo–western Pacific climate during the summer following El
906 Niño. *J Clim* 22: 730–747

907 Xing W, Wang B, Yim SY (2016) Peak-summer East Asian rainfall predictability and
908 prediction part I: Southeast Asia. *Clim Dyn* 47:1–13

909 Yang S, Zhang Z, Kousky VE, Higgins RW, Yoo SH, Liang J, Fan Y (2008)
910 Simulations and seasonal prediction of the Asian summer monsoon in the NCEP
911 climate forecast system. *J Clim* 21: 3755–3775

912 Yim SY, Jhnu JG, Lu R, Wang B (2010) Two distinct patterns of spring Eurasian snow
913 cover anomaly and their impacts on the East Asian summer monsoon. *J Geophys*
914 *Res* 115: D22113

915 Yim SY, Wang B, Xing W (2016) Peak-summer East Asian rainfall predictability and
916 prediction part II: Extratropical East Asia. *Clim Dyn* 47: 15–30

917 Ying K, Zheng X, Zhao T, Frederiksen CS, Quan X-W (2017) Identifying the
918 predictable and unpredictable patterns of spring-to-autumn precipitation over
919 eastern China. *Clim Dyn* 48: 3183–3206

920 Ying K, Frederiksen CS, Zhao T, Zheng X, Xiong Z, Yi X, Li C (2018) Predictable
921 and unpredictable modes of seasonal mean precipitation over Northeast China.
922 *Clim Dyn* 50: 3081–3095

923 Zhang W, Huang Z, Jiang F, Stuecker MF, Chen G, Jin FF (2021) Exceptionally
924 persistent Madden–Julian Oscillation activity contributes to the extreme 2020
925 East Asian summer monsoon rainfall. *Geophys Res Lett* 48: e2020GL091588

926 Zheng F, Li J, Li Y, Zhao S (2016) Influence of the summer NAO on the
927 spring–NAO–based predictability of the East Asian summer monsoon. *J Appl*
928 *Meteorol Clim* 55: 1459–1476

929 Zheng X, Frederiksen CS (2004) Variability of seasonal-mean fields arising from
930 intraseasonal variability: Part 1. Methodology. *Clim Dyn* 23:171–191

931 Zheng X, Frederiksen CS (2006) A study of predictable patterns for seasonal
932 forecasting of New Zealand rainfall. *J Clim* 19:3320–3333

933 Zheng X, Straus DM, Frederiksen CS (2008) Variance decomposition approach to the
934 prediction of the seasonal mean circulation: Comparison with dynamical
935 ensemble prediction using NCEP’s CFS. *Q J R Meteorol Soc* 134: 1997–2009

936 Zhou Q, Zhang R (2021) Possible impacts of spring subtropical Indian Ocean Dipole
937 on the summer tropical cyclone genesis frequency over the western North Pacific.
938 *Int J Climatol*. Doi: 10.1002/joc.7539

939 Zhou ZQ, Xie SP, Zhang R (2021) Historic Yangtze flooding of 2020 tied to extreme
940 Indian Ocean conditions. *Proc Natl Acad Sci* 118: e2022255118

941

942 **Table 1.** The explained variance percentage of the EASMR P-PCs, T-PCs and RP-PCs
 943 in each individual component (EV; unit: %), and the potential predictability [PP;
 944 unit: %; Eq. (6)] of each PC; and the cumulative variance percentage of the total
 945 seasonal mean EASMR explained by the leading P-PCs, T-PCs and RP-PCs in their
 946 corresponding total [AEV.t; unit: %; Eq. (7)], predictable [AEV.p; unit: %; Eq. (8)]
 947 and unpredictable [AEV.u; %; Eq. (9)] components, respectively, for the period
 948 1979–2019.

EASMR PCs	EV (%)	PP (%)	AEV.t (%)	AEV.p (%)	AEV.u (%)
P-PC1	22	63	16	10	6
P-PC2	13	80	25	17	8
P-PC3	9	85	31	23	9
P-PC4	8	44	38	25	13
P-PC5	7	59	42	28	14
P-PC6	5	60	46	31	15
T-PC1	21	38	21	8	13
T-PC2	11	50	31	13	18
T-PC3	8	10	39	14	25
T-PC4	7	65	46	18	28
T-PC5	6	44	52	21	31
T-PC6	5	22	57	22	35
RP-PC1	31	65	9	6	3
RP-PC2	25	60	16	10	6
RP-PC3	18	72	21	14	7
RP-PC4	14	75	25	17	8

949

950

951 **Table 2.** Summary of the seasonal predictors for EASMR used in this work.
 952

Predictor	Definition
DC ENSO	<i>November-to-March</i> Niño1+2 [90°–80°W, 10°S–0°] SST (Trenberth 1997)
Spring AO	<i>April–May</i> AO index (Higgins et al. 2002)
DV ENSO	<i>May</i> Niño4 [160°E–150°W, 5°S–5°N] SST (Trenberth 1997)
Western North Pacific SST	<i>April–May</i> detrended SST in [120°–150°E, 0°–20°N]
Southern Atlantic SST	<i>March–April</i> detrended SST in [60°–30°W, 30°–45°S]
Trend	Consecutive years from 1 to 41
Tropical Southern Atlantic SST	<i>May</i> detrended SST in [30°W–10°E, 0°–20°S]
Southern Indian SST	<i>March</i> SST differences between [80°–140°E, 15°–65°S] and [45°–80°E, 30°–55°S]
Arctic Ocean SST	<i>March–April–May</i> SST in [20°–150°E, 70°–90°N]

953

Note: For the last six climate indices, the DC/DV ENSO and spring AO signals are removed using linear regression (as in Section 2.2.1, but for climate indices)

954

955

956

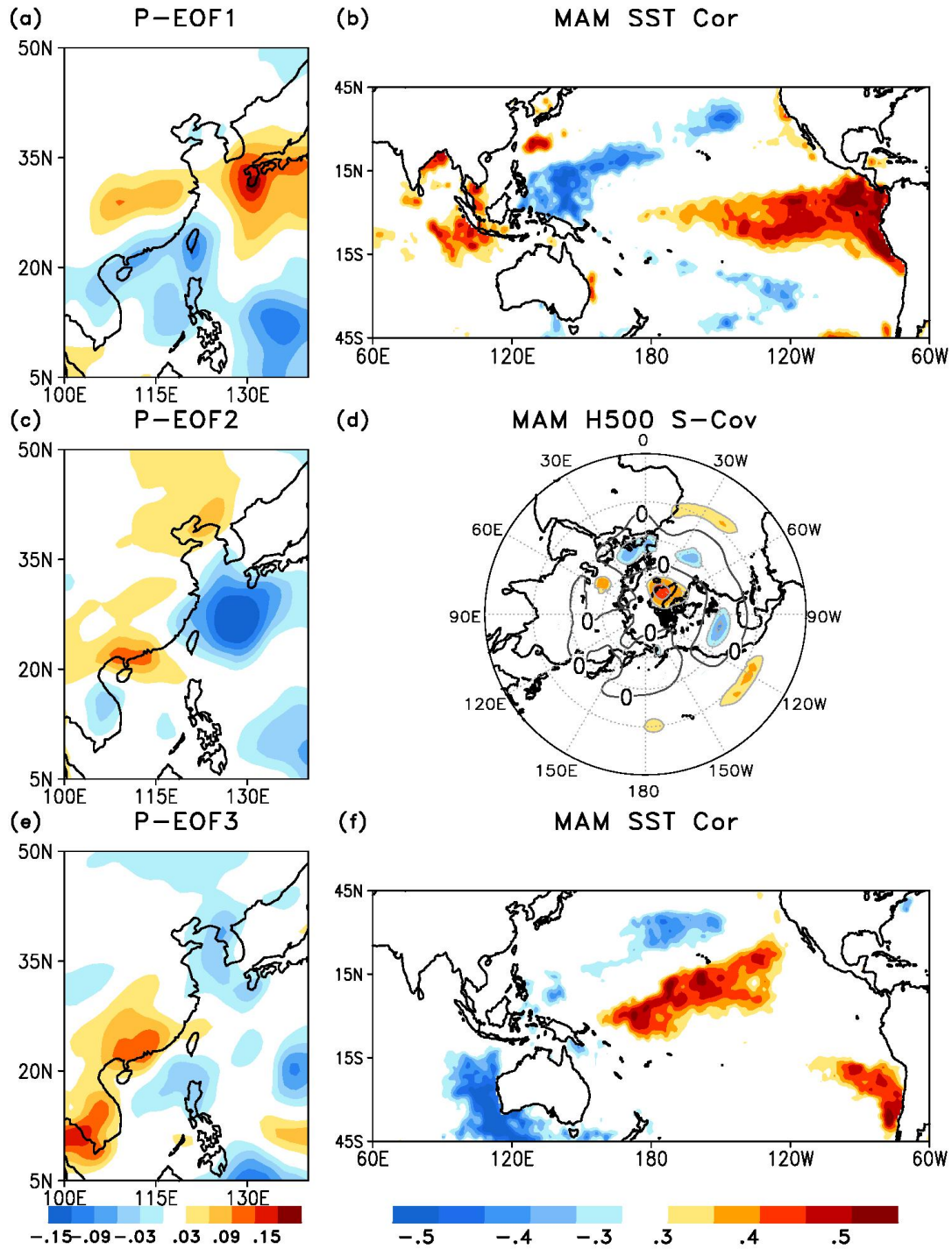
957 **Table 3.** Averaged fraction variance skill [FV; unit: %; Eq. (5)] for total seasonal
958 mean EASMR explained by the observation, and the cross-validated PC regression
959 schemes (scheme-*AB*, -*A* and -*B*) for the period 1979–2020 over the whole of East
960 Asia, land areas only, and ocean areas only.

961

Scheme	FV (whole area)	FV (land only)	FV (ocean only)
Obs	28	24	29
Scheme- <i>AB</i>	26	23	28
Scheme- <i>A</i>	11	8	13
Scheme- <i>B</i>	15	15	15

962

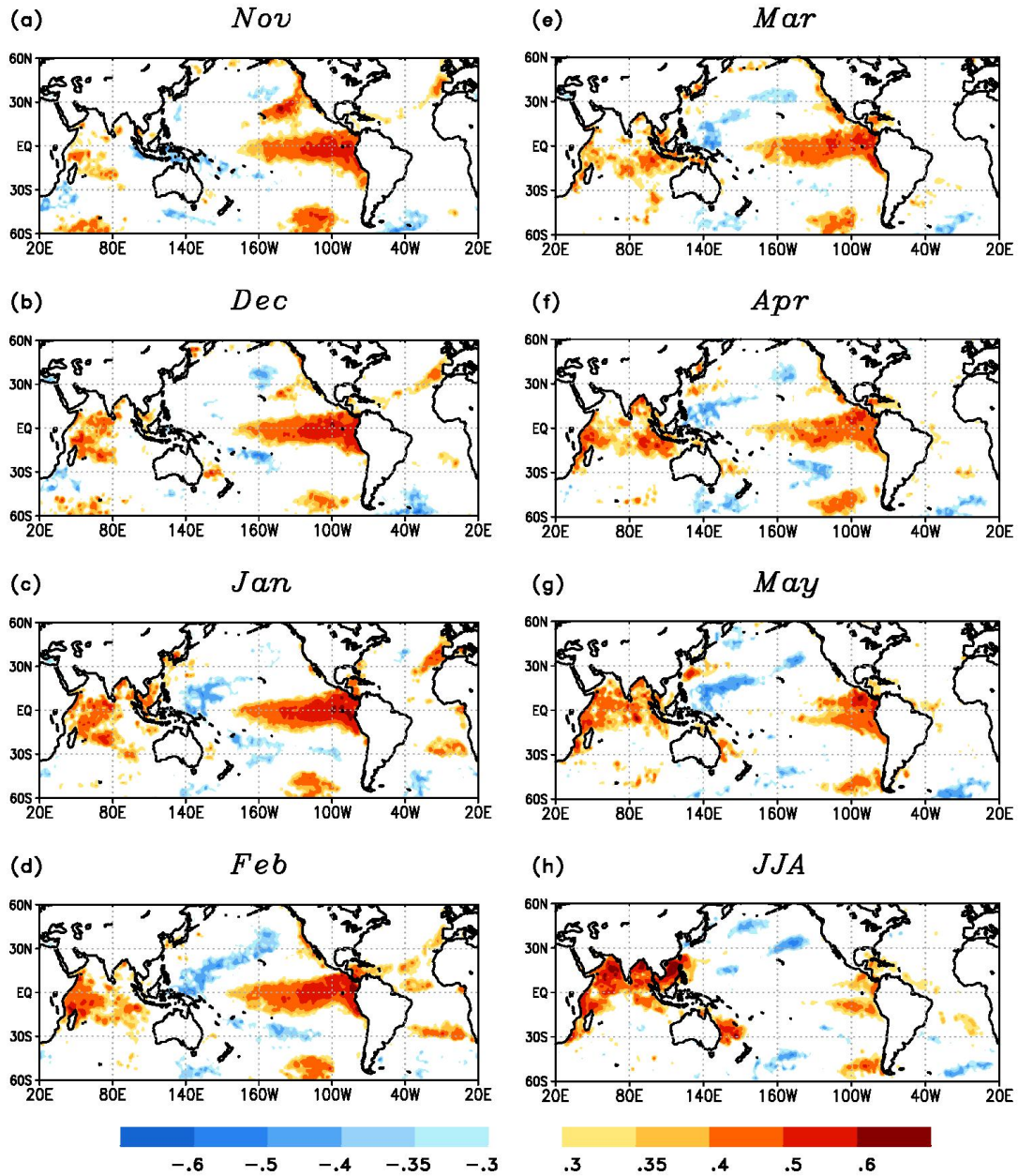
963



964

965 **Fig. 1.** (a, c, e) Spatial distributions of the leading three predictable modes (P-EOFs)
 966 of EASMR and (b, d, f) the SST correlation maps or the 500 hPa height slow or
 967 predictable covariance maps [Eq. (3)] at a one-season lead (March–April–May)
 968 associated with the leading three P-EOFs during 1979–2019. The shaded areas in the
 969 correlation and covariance maps are significant at the 95% confidence level according
 970 to the Student's t -test and χ^2 test, respectively.
 971

P-PC1 SST Cor



972

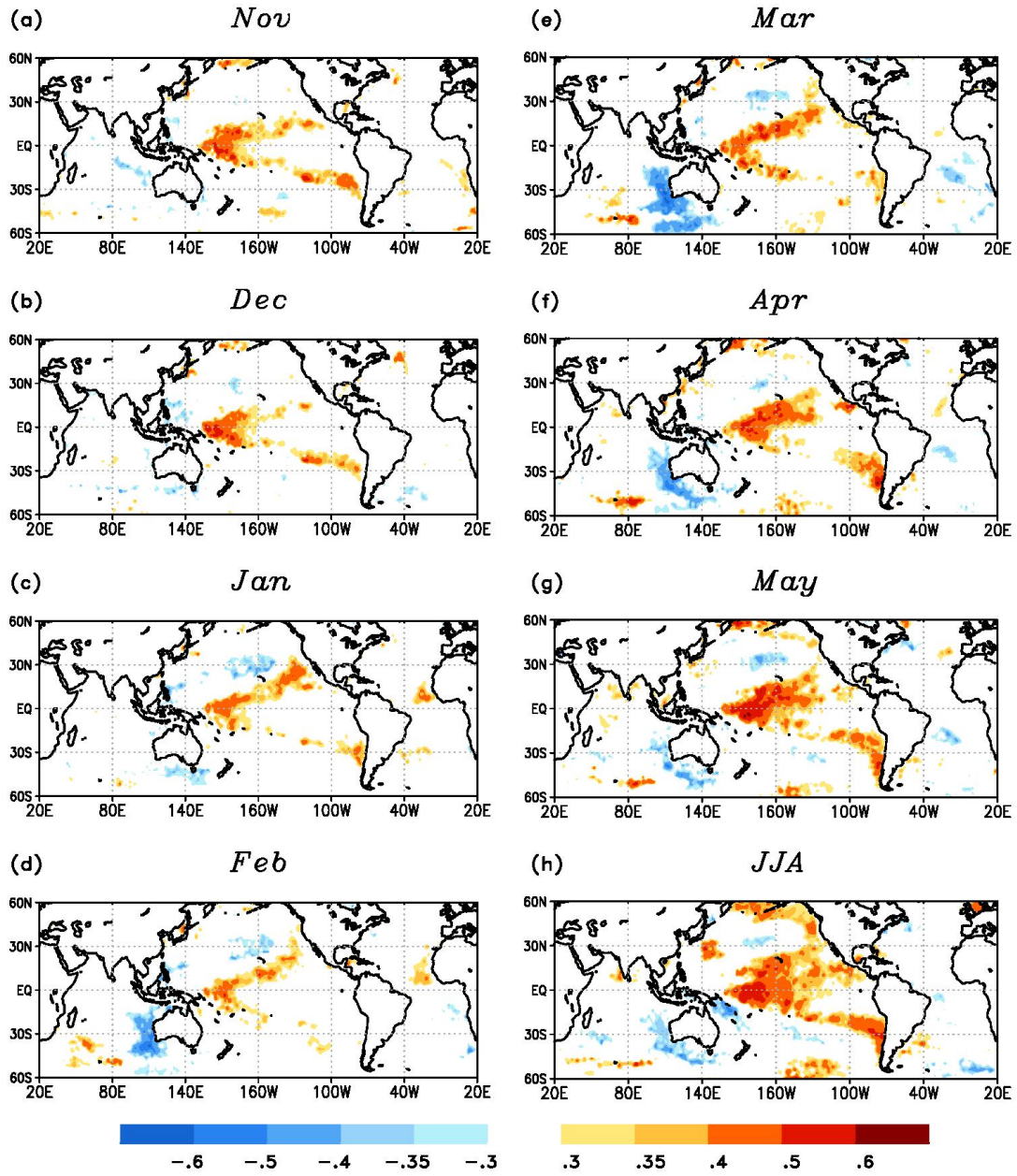
973 **Fig. 2.** One-point correlations between EASMR P-EOF1 and the global SST in the
974 preceding (a) November, (b) December, (c) January, (d) February, (e) March, (f) April
975 and (g) May, and (h) current JJA, during 1979–2019. The shaded areas are significant
976 at the 95% confidence level according to the Student's *t*-test.

977

978

979

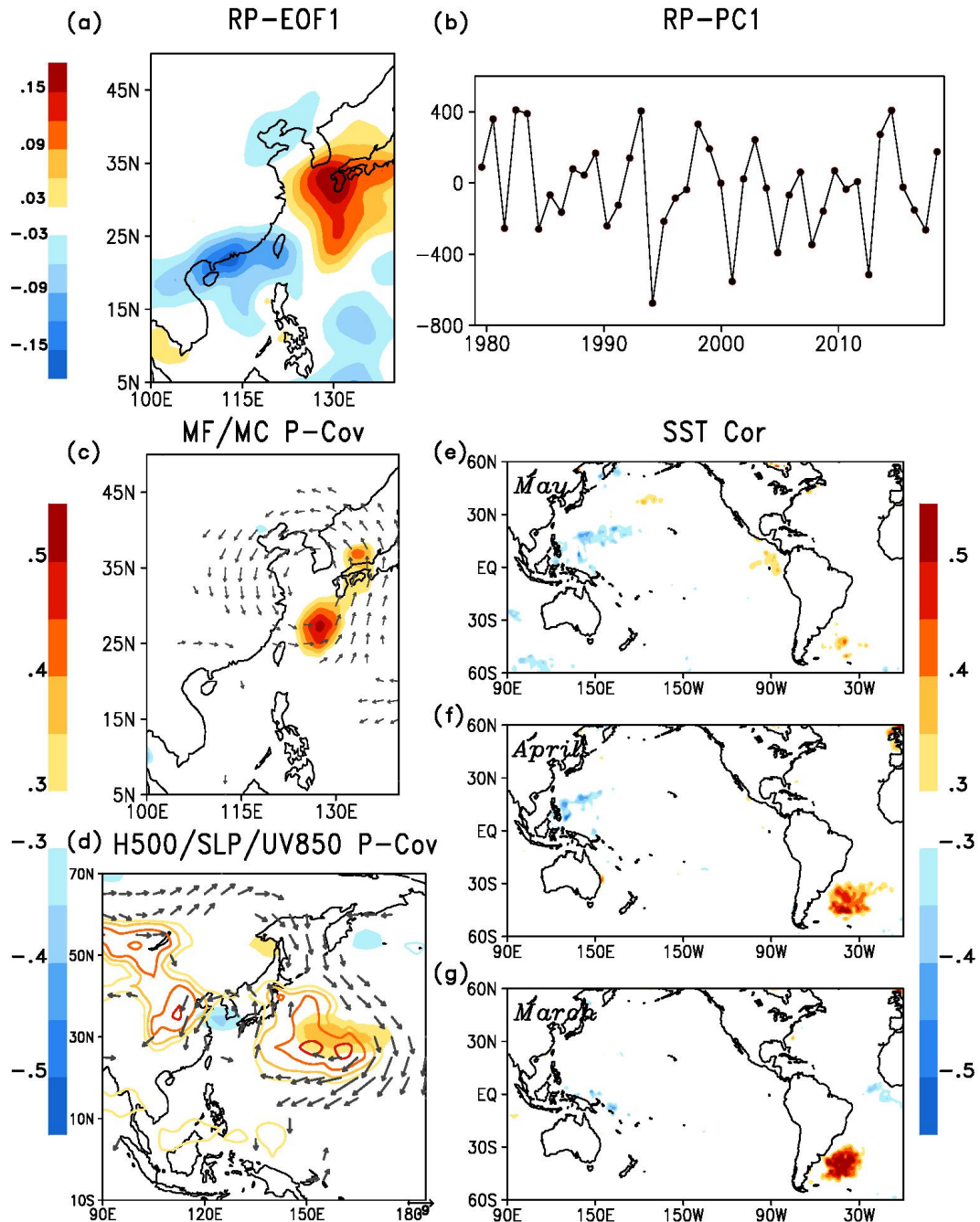
P-PC3 SST Cor



980

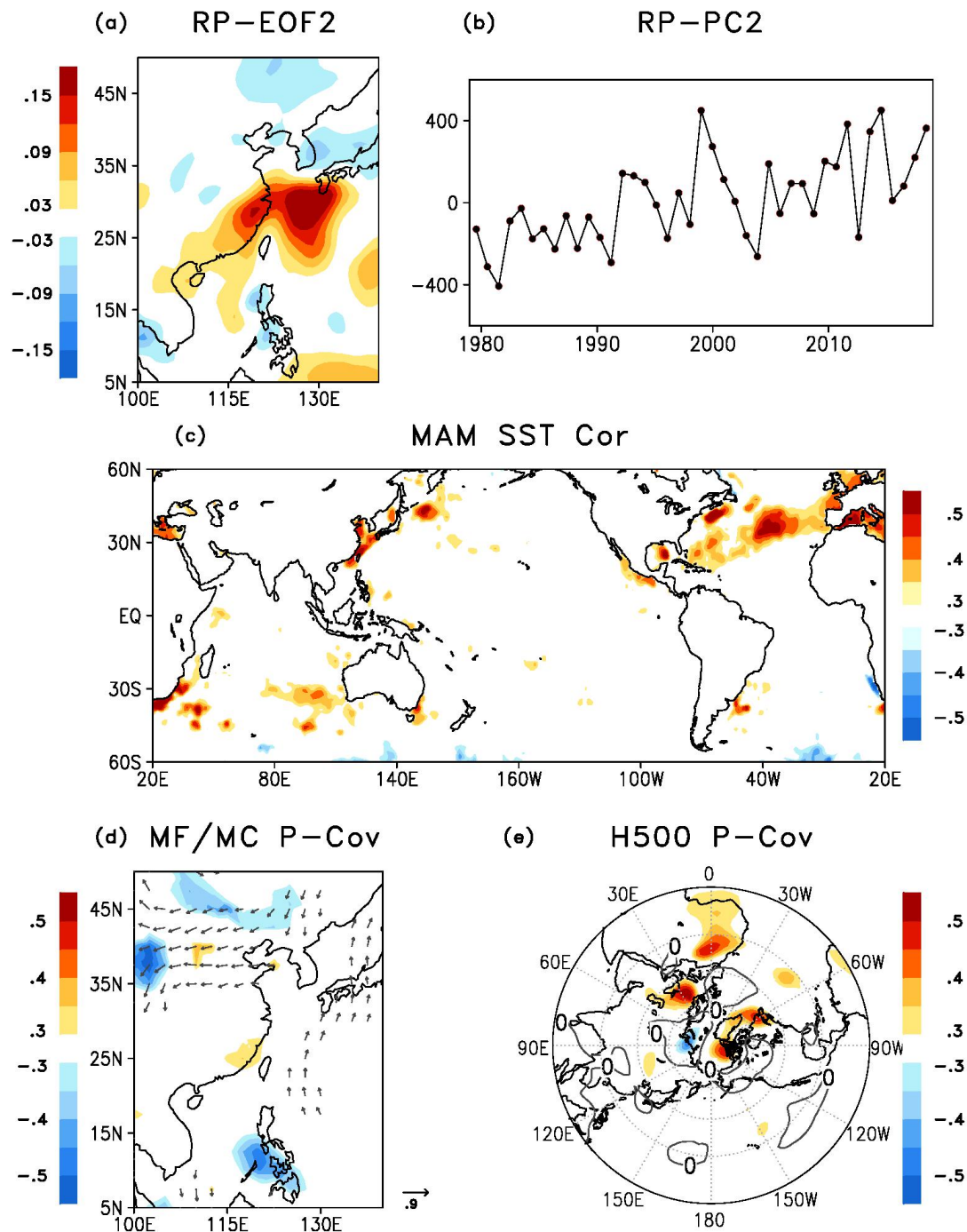
981 **Fig. 3.** As in Fig. 2 but for EASMR P-EOF3.

982



983

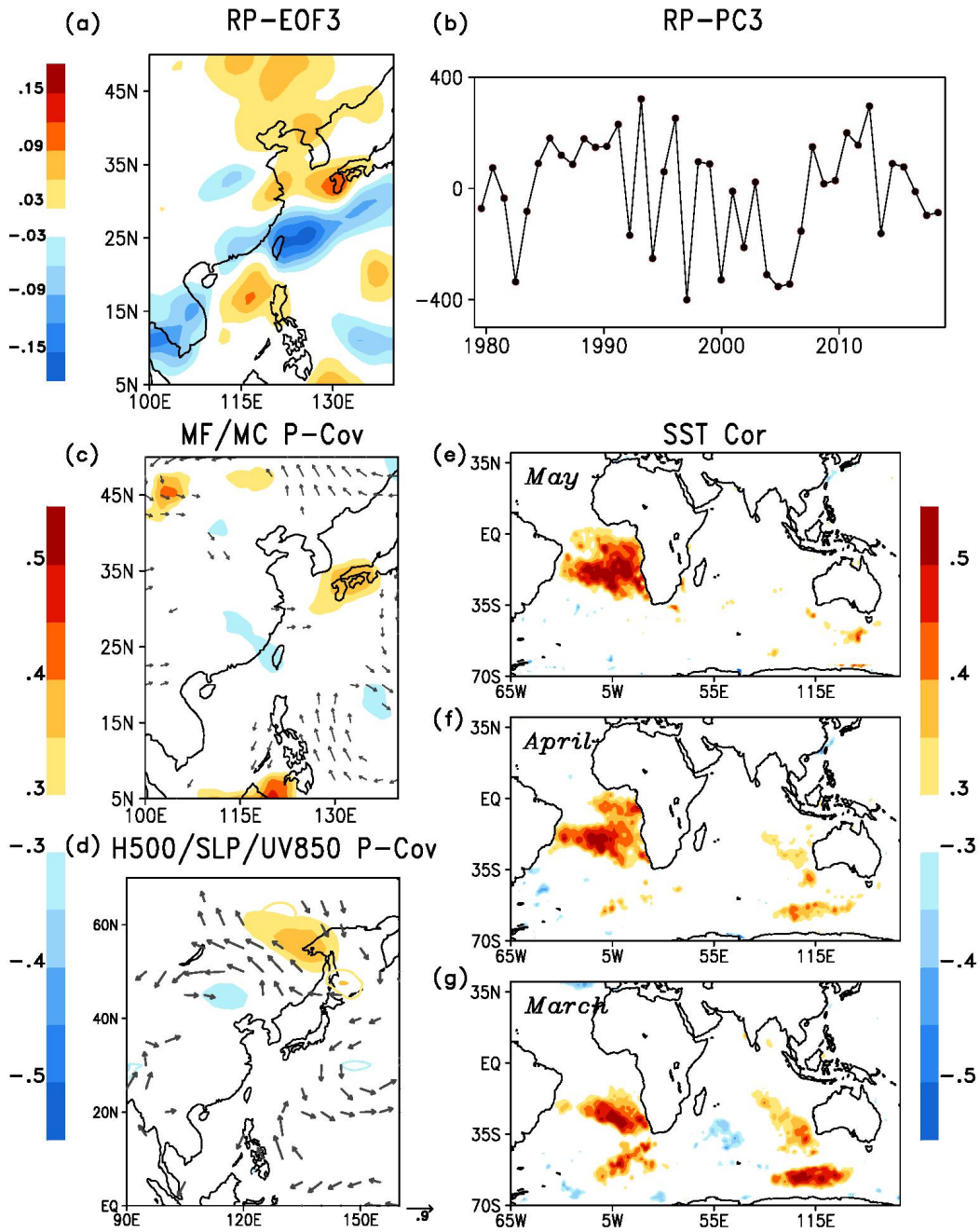
984 **Fig. 4.** The (a) spatial and (b) temporal patterns of EASMR RP-EOF1; the slow or
 985 predictable covariance [Eq. (3)] between the PC time series for the RP-EOF1 and (c)
 986 the simultaneous vertically integrated (at 300, 400, 500, 600, 700, 850, 925 and 1000
 987 hPa) moisture flux (*vector plots*) and moisture convergence (*shaded plots*), and (d)
 988 the simultaneous 500 hPa geopotential height (*shaded plots*), sea level pressure
 989 (*contour plots*) and horizontal wind at 850 hPa (*vector plots*); and the one-point
 990 correlations between EASMR RP-EOF1 and the global SST in the preceding (e) May,
 991 (f) April and (g) March, during 1979–2019. The shaded areas in the SST correlation
 992 map are significant at the 95% confidence level according to the Student's *t*-test. The
 993 shaded areas and the vectors in the covariance maps are significant at the 95%
 994 confidence level using the χ^2 test.



995

996 **Fig. 5.** The (a) spatial and (b) temporal patterns of EASMR RP-EOF2; (c) the
 997 one-point correlation of the March–April–May (MAM) SST associated with
 998 RP-EOF2, and the slow or predictable covariance [Eq. (3)] between the PC time
 999 series for RP-EOF2 and (d) the simultaneous vertically integrated (at 300, 400, 500,
 1000 600, 700, 850, 925 and 1000 hPa) moisture flux (*vector plots*) and moisture
 1001 convergence (*shaded plots*), and (e) the simultaneous 500 hPa geopotential height,
 1002 during 1979–2019. The shaded areas in the SST correlation map are significant at the
 1003 95% confidence level according to the Student’s *t*-test. The shaded areas and the
 1004 vectors in the covariance maps are significant at the 95% confidence level using the χ^2
 1005 test.

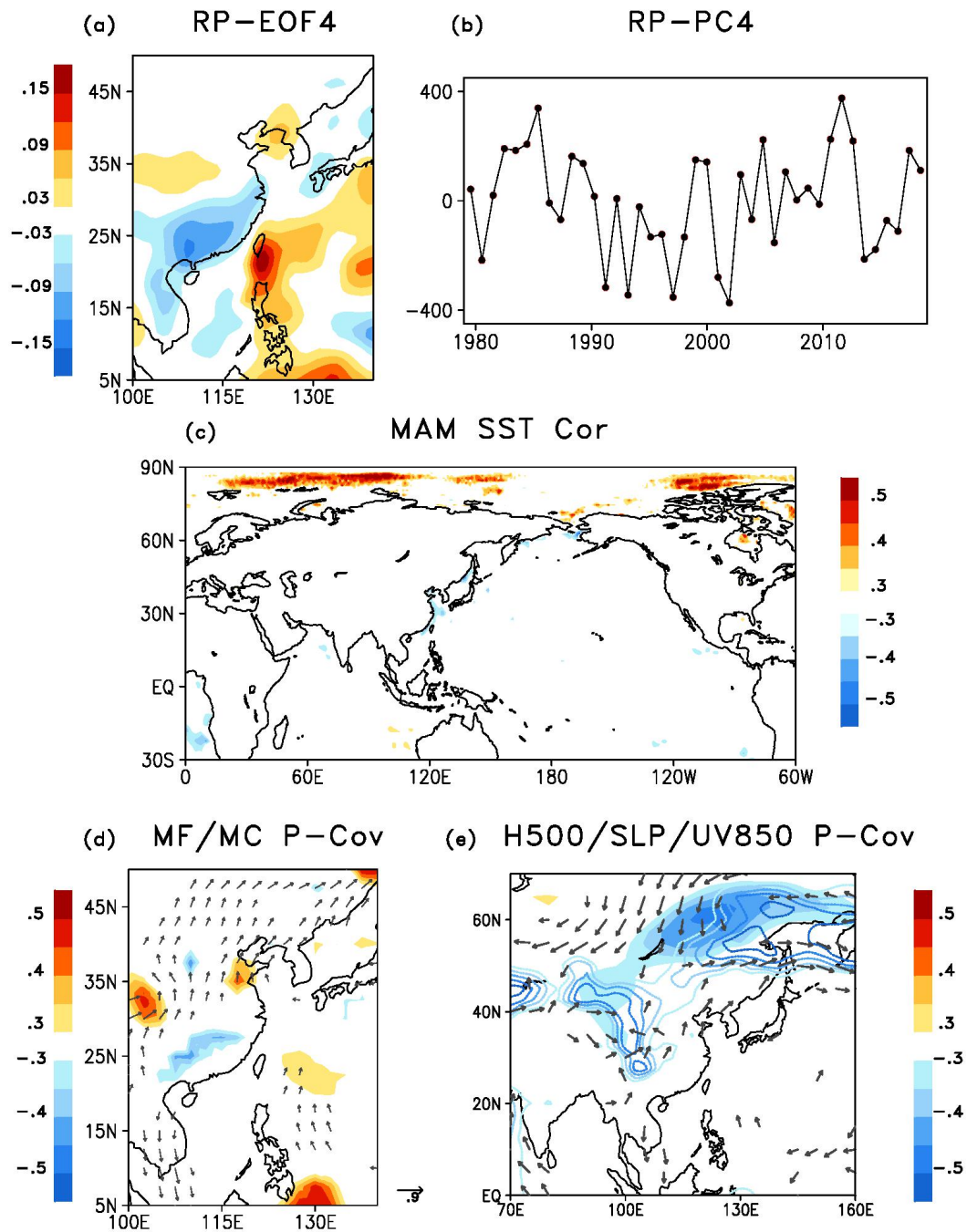
1006



1007

1008 **Fig. 6** The (a) spatial and (b) temporal patterns of EASMR RP-EOF3; the slow or
 1009 predictable covariance [Eq. (3)] between the PC time series for RP-EOF3 and (c) the
 1010 simultaneous vertically integrated (at 300, 400, 500, 600, 700, 850, 925 and 1000 hPa)
 1011 moisture flux (*vector plots*) and moisture convergence (*shaded plots*), and (d) the
 1012 simultaneous 500 hPa geopotential height (*shaded plots*), sea level pressure (*contour*
 1013 *plots*) and horizontal wind at 850 hPa (*vector plots*); and the one-point correlations
 1014 between EASMR RP-EOF3 and the global SST in the preceding (e) May, (f) April
 1015 and (g) March, during 1979–2019. The shaded areas in the SST correlation map are
 1016 significant at the 95% confidence level according to the Student's *t*-test. The shaded
 1017 areas and the vectors in the covariance maps are significant at the 95% confidence
 1018 level using the χ^2 test.

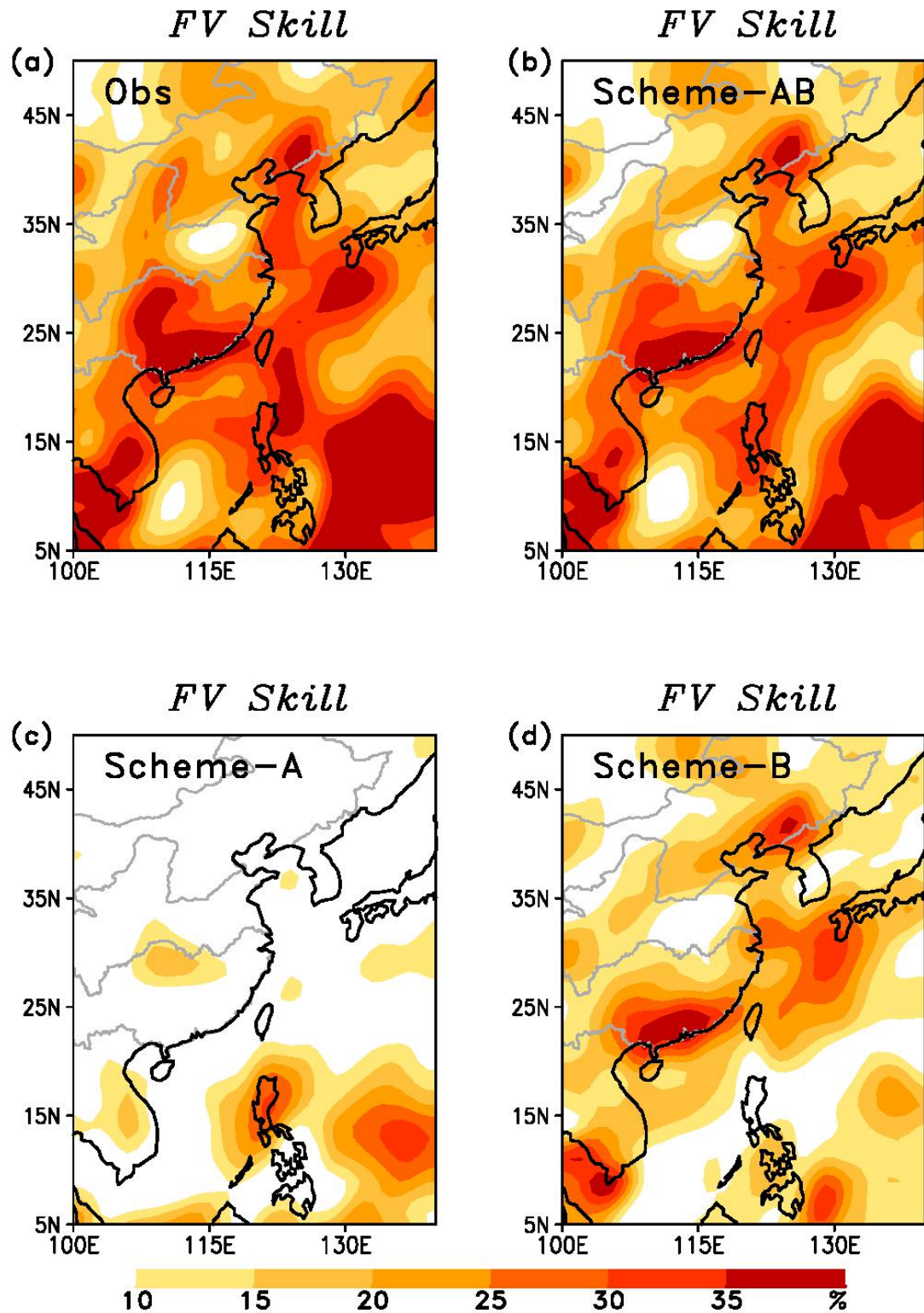
1019



1020

1021 **Fig. 7.** The (a) spatial and (b) temporal patterns of EASMR RP-EOF4; (c) the
 1022 one-point correlation of the March–April–May (MAM) SST associated with
 1023 RP-EOF4, and the slow or predictable covariance [Eq. (3)] between the PC time
 1024 series for RP-EOF4 and (d) the simultaneous vertically integrated (at 300, 400, 500,
 1025 600, 700, 850, 925 and 1000 hPa) moisture flux (*vector plots*) and moisture
 1026 convergence (*shaded plots*), and (e) the simultaneous 500 hPa geopotential height
 1027 (*shaded plots*), sea level pressure (*contour plots*) and horizontal wind at 850 hPa
 1028 (*vector plots*), during 1979–2019. The shaded areas in the SST correlation map are
 1029 significant at the 95% confidence level according to the Student’s *t*-test. The shaded
 1030 areas and the vectors in the covariance maps are significant at the 95% confidence
 1031 level using the χ^2 test.

1032



1033

1034 **Fig. 8.** Spatial distributions of the fraction variance skill [FV; unit: %; Eq. (5)] of the
 1035 total seasonal mean EASMR explained by the (a) observation, and the cross-validated
 1036 PC regression schemes (b) -AB, (c) -A and (d) -B, respectively, during 1979–2020.

1037

Supplementary Files

This is a list of supplementary files associated with this preprint. Click to download.

- [supplementaryinformation.pdf](#)